science.sciencemag.org/content/372/6537/63/suppl/DC1

Supplementary Materials for

Extinction at the end-Cretaceous and the origin of modern Neotropical rainforests

Mónica R. Carvalho*, Carlos Jaramillo*†, Felipe de la Parra, Dayenari Caballero-Rodríguez, Fabiany Herrera, Scott Wing, Benjamin L. Turner, Carlos D'Apolito, Millerlandy Romero-Báez, Paula Narváez, Camila Martínez, Mauricio Gutierrez, Conrad Labandeira, German Bayona, Milton Rueda, Manuel Paez-Reyes, Dairon Cárdenas, Álvaro Duque, James L. Crowley, Carlos Santos, Daniele Silvestro

*These authors contributed equally to this work.
†Corresponding author. Email: jaramilloc@si.edu

Published 2 April 2021, *Science* **372**, 63 (2021)
DOI: 10.1126/science.abf1969

This PDF file includes:

Other Supplementary Materials for this manuscript include the following:
(available at science.sciencemag.org/content/372/6537/63/suppl/DC1)

Data S1 to S6

Materials and Methods

Palynological dataset

The complete dataset consisted on 75,567 occurrences of terrestrial palynomorphs counted from 645 palynological samples. These were sampled from 39 stratigraphic sections obtained from wells and outcrops that encompass the Maastrichtian-Paleocene time span (Table S1; Data S1; Fig. 1). Pollen samples were prepared at Paleoflora, Bucaramanga, Colombia, following standard palynological techniques of digesting sediments in mineral acids (HF and HCl), alkaline treatment in KOH, heavy liquid separation using $ZnBr_2$ and sieving (*66*). At least 200 palynomorph grains were counted per sample when possible. Dating of the samples was done using Graphic Correlation (*67*) on the palynological data using a biostratigraphic zonation for the region that is calibrated with magnetostratigraphy, carbon isotopes, and foraminifera (*68*). Graphic correlation (*67*, *69*, *70*) has been extensively used over the past decades in multiple studies (*68*, *71–74*). Graphic correlation does not make the *a priori* assumption that first (FAD) and last appearance datums (LAD) in a section record speciation and extinction events. It combines the information of multiple sections to find the true stratigraphic range of a taxon; therefore, the use of an "index" fossil is not necessary because the whole assemblage is being compared. The graphic correlation analysis was done using GraphCor (*75*). We used the Standard Composite Section (SCS) of Jaramillo et al. (*25*) to produce a Composite Unit (DUC) for each of the samples analyzed. Each DUC was dated using the calibration of Jaramillo et al. (*68*) with a few additional calibration points (Table S2) and assuming a linear sedimentation rate between the calibration points of the SCS. It is reasonable to assume linearity because the SCS does not have major stratigraphic breaks. The geological time scale follows Gradstein et al. (*76*) and Hilgen et al. (*77*). It is important to stress that ages provided in this research are relative, and the precision goes as far as the calibration points for the zonation. We do not argue that our ages are precisely calibrated with the geological time record, but they indicate a relative age compared to sediments above and below. These ages represent a hypothesis that could change as more calibration points are added to the zonation or if a calibration point is shifted or the line of correlation of each section is modified. Our ages are fully replicable as we provide DUC and the calibration points of the SCS. Occurrences were organized into an abundance matrix (R Code available in Figshare digital repository, doi: 10.6084/m9.figshare.13611215).

Samples with relative abundance of marine elements and/or reworked material above 10% were excluded. Although this study focuses only in the Maastrichtian-Paleocene (72-58 Ma, referred as K-Pg hereafter), our full dataset extends from 122.8 to 0 Ma. To eliminate false FAD or LADs produced by selecting only the 72-58 Ma interval, we added two extra samples to the 72-58 Ma dataset. These samples contain the taxa that extend their range in younger strata (sample 0 Ma) or older strata (sample 123 Ma).

For all of the following analyses (except for cohort survivorship and PyRate analyses, see below), individual samples were grouped into time-bins in order to reduce the bias by differences in sampling density and sample counts along the stratigraphic profile. Time-bins were selected based on a minimum number of palynomorph occurrences. The sum of occurrences within each bin included >1,000 palynomorphs, which resulted in the 17 time-bins that are shown in the right column of Fig. 2. All analyses were performed using *R for Statistical Computing* (*78*). Statistical analyses were performed using two-sided Student t-tests or Wilcoxon tests, with $\alpha = 0.05$ to evaluate the equality of means. The degrees of freedom (*df*) were calculated using the Welch modification to account for different variances in the groups being compared and *p*-values are reported for each test at the appropriate point. For all correlations we report the Spearman's rank-

order correlation ρ and *p*-values. A subset of the full dataset, named hereafter "Culled dataset" was also produced by excluding a set of taxa that were uninformative for diversity analysis (e.g. *Psilatriletes* sp., *Psilatricolpites sp*.). The culled set contains 637 samples, 1,048 taxa and 53,029 occurrences.

Cluster, DCA, and pollen composition

We performed a cluster analysis using the Sørensen's coefficient and the Unweighted Pair-Group Method using Arithmetic Averages (packages "philentropy", "dendextend" and "cluster" (*79–81*). We used the Culled dataset after applying a range-through (*82*). The comparison was also performed on individual samples excluding those with counts < 40 grains/sample and resultant nodes were ordered by the mean age of the branches (package "dendextend") (*80*) (Fig. S1). We also performed a Detrended Correspondence Analysis (DCA) (*83*) using the package "vegan" (*84*) on individual samples excluding those with counts < 40 grains/sample. Palynomorphs were grouped into three broad taxonomic categories including pteridophytes, gymnosperms [gnetales + conifers] and angiosperms. Changes in proportions were calculated using the complete database but excluding samples with counts <100 grains/sample (Fig. S2).

Palynological Diversity

Diversity analyses were performed on the Culled dataset using the package "divDyn" (*85*)(Table S3). We used the Corrected sampled-in-bin diversity (richness) of Alroy (*20*) and the Second-for-third extinction and origination rates of Alroy (*22*). Resampling was performed to assess the significance of the estimated diversity parameters (*86*). We subsampled 300 times using a shareholder quorum subsampling (SQS) (*21*) of >= 0.95.

A cohort survivorship analysis (*87*) was done on the Culled dataset, using 1–My time bins in order to have equal time representation in each bin. Cohorts are defined as groups of palynomorphs that coexist at a given time in this analysis. The changes in numbers of individual cohorts present in each bin (=slopes) were represented as boxplots in Fig. 2E. We did a Spearman correlation between diversity indicators versus 1) the geographic area covered by each estimating the area (km^2) corresponding to the minimum polygon that included all localities represented on each time bin (package "geosphere") (*88*); 2) bin duration; and 3) sedimentary facies of the samples (Table S4).

We inferred origination and extinction rates from the culled pollen dataset using the Bayesian framework implemented in the program PyRate (*23*), which jointly estimates the times of origination and extinction for all taxa, preservation, and origination and extinction rates through time. We excluded singletons. To account for age uncertainties and assess convergence among different runs, we randomized the age of each fossil occurrence within a range of +/- 0.01 Myr and ran 10 independent runs. We analyzed each dataset using the reversible jump Markov chain Monte Carlo algorithm (RJMCMC) which estimates rate shifts in origination and extinction rates in continuous time sampling their number and temporal placement from their posterior distribution. We use a time-variable preservation model (*23*) with independent rates inferred within 1-Myr time bins. To control for over-parameterization we assigned all preservation rates a gamma prior with fixed shape parameter (alpha = 2) and an estimated rate parameter with an exponential prior density. We ran the analyses of the 10 replicated datasets for 25 million RJMCMC iterations, with a sampling frequency of 10,000 and summarized the combined the output to produce rates-through time plots (Figs. 2, S3). Marginal rates were summarized as mean and 95% credible intervals within arbitrarily small time bins (0.05 Myr)

and we assessed the significance of rate shifts by computing log Bayes factors based on their posterior frequency and their prior expectation (Fig. S3). The input file and complete list of commands utilized for the PyRate analyses are available in Figshare digital repository, doi: 10.6084/m9.figshare.13611215).

There is a peak in origination rate observed at 62–63 Ma in the divDyn analysis that is also observed in PyRate, although with large credible intervals (CI: 0.05–0.35). This result could be a sampling size artifact and subsampling indicates that origination rate at this bin might be actually lower than average (300 iterations, SQS 0.95, 0.07 vs 0.09, t-test, df = 342.2, P= 0.1255). Neither origination nor extinction rates are correlated to either bin span (ρ = -0.06, P = 0.81; ρ = -0.04, P = 0.89 respectively), or area size (ρ = 0.05, P = 0.8351, ρ = -0.14, P = 0. 5684) in this analysis. Given the large amount of fossil data and high precision of the estimated ages of the occurrences, we repeated the PyRate analyses allowing for higher resolution in the RJMCMC search for rate shifts. To achieve that, we set the prior on the size of time windows between rate shifts (which prevents rate shifts from being temporally too close potentially causing numerical overflows) to 0.2 Myr. This analysis allowed us to assess the robustness of the results against a different granularity of the RJMCMC search and to verify whether short but significant rate shifts emerge when increasing the resolution of the analysis.

Leaf macrofossils

We collected 4,469 leaf fossils from three sites of the Maastrichtian Guaduas Formation and five sites of the Paleocene lower Bogotá Formation (Table S5; Data S2). Collections were made from a varying number of quarries as a means to represent lateral variability. All fossil sites of the Guaduas and Bogotá Fm. occur in floodplain deposits and represent autochthonous leaf assemblages with little transportation. In two sites of the Guaduas Formation (Montecristo and 860017Ce) and one site from the Bogotá Formation (0903Ce), leaves were collected as unbiased field censuses (Table S5). Over 500 identifiable leaf specimens were recorded from a single leaf bed to be further used in comparisons of floristic composition.

All fossils were studied under permits MGJRG-048-08, MGJRG-050-08, MGJRG-051-08, MGJRG-052-08, SGB-MGN-124-09, SGB-MGN-174-09, SGB-MGN-201-09 and SGB-MGN-947-12, granted by the Colombian Geological Service (former Ingeominas) between 2008-2012. Fossil specimens are deposited in the collections of the Museo Mapuka, Universidad del Norte in Baranquilla, Colombia and at the Museo Paleontológico José Royo y Gómez, Colombian Geological Service in Bogotá, Colombia.

An additional 2,482 leaf fossils previously reported from the Mid-Late Paleocene Cerrejón Formation (*19*) were also included in our leaf fossil dataset (Table S5). Additional information on the fossil material can be accessed using specimen STRI-id numbers through: https://biogeodb.stri.si.edu/jaramillosdb/web/.

Dating of fossil sites

Sediments from fossil sites were dated using the palynological zonation of Jaramillo et al., (*68*), which indicated a Maastrichtian age for all Guaduas sites and middle-late Paleocene age for all Bogotá sites. An additional radiometric age obtained from a stratigraphic meter 928 at the type section of the Bogota formation (*89*) using CA-TIMS $^{206}Pb/^{238}U$ yielded an age of 60.79 ± 0.02 Ma (MSWD = 0.9) (Data S3) confirming a Paleocene age for the Bogota Formation macrofossils. Radiometric dating was performed via laser ablation inductively coupled plasma

mass spectrometry (LA-ICPMS) and chemical abrasion isotope dilution thermal ionization mass spectrometry (CA-TIMS) at Boise State University.

Leaf physiognomy and paleoprecipitation estimates

Leaves were classified into discrete morphotypes and described following the Manual of Leaf Architecture (*90*) (Data S4–S5). For each morphotype, leaf size was scored following the Raunkiaer-Webb size categories (*91*, *92*) (Tables S6–S7) and was used to provide estimates of mean annual precipitation (Table S8) using both the leaf area analysis method of Wilf et al. (*28*) and regression proposed by Peppe et al. (*29*).

Leaf Mass per Area

We estimated leaf mass per area (LMA) for morphotypes of the Guaduas and Bogotá floras using the procedures described by Royer et al. (*30*), which are based on biomechanical relationships between leaf size and petiole cross-section. Only complete or nearly complete leaf fossils (having both margins and petiole) were selected. Leaf shape was digitally reconstructed for nearly complete leaves, and lamina area and petiole width were quantified photos using ImageJ.

Morphotype and site mean LMA, and 95% prediction intervals were estimated following the methods and equations described in (*30*) (Fig. S4; Table S9). The mean values of LMA per site were calculated using leaf morphotypes represented by two or more specimens, and site-means compared among floras using an unpaired t-test (Table S10).

Floristic comparison between Maastrichtian, Paleocene and living Neotropical rainforests

We compared all leaf morphotypes with cleared leaves from the National Cleared Leaf Collection through the ClearedLeafDB (*93*) and revised previously described taxa from the Bogotá and Guaduas floras (*32–35*, *94*, *95*). Following Wing et al. (*19*), the general resemblance of fossil leaves to modern angiosperm families was established based on the overall morphological similarity between a leaf morphotype and several lineages within a given family ("best guess"), whereas natural affinities were established when two or more leaf traits were consistently found within a plant family and were shared with any given leaf morphotype (Tables S6–S7). Among the leaf taxa that have been previously described from the Guaduas Formation (*32*, *33*, *94*), we were unable to confirm the familial affinities of *"Ficus" andrewsi* Huert. given that most of the morphological characters that distinguish this taxon are found across numerous unrelated lineages of angiosperms. Other unconfirmed familial affinities include those of Berry's (*96*)*"Nectandra" areolata* Engelhart, "*Coussapoa" ampla* Berry and *Theobroma fossillium* Berry, described from sediments surrounding Tequendama that were later identified to be from the Guaduas Formation (*94*). Among these, *"Coussapoa" ampla* and *"Nectandra" aerolata* were identified based on incomplete leaf specimens and were therefore not comparable with our leaf morphotype system nor could their familial affinities be confirmed. Similarly, Brown (*97*) indicated that the fossil fruit described as *Theobroma fossillium* is not a plant but rather a concretion enclosing a vertebrate jaw fragment and therefore macrofossil evidence of Malvaceae is unconfirmed in the Guaduas Formation.

The occurrence of dominant plant families in modern Neotropical rainforests was examined in the Maastrichtian Guaduas flora and the Paleocene Bogotá and Cerrejón floras, using 72 Neotropical rainforest plots from the Alwyn H. Gentry Forest Transect Data Set as a reference (*98*). These transect data are available at

http://www.mobot.org/mobot/research/gentry/welcome.shtml. Only plots below altitudes of 1000 m and with precipitation exceeding 180 cm/yr were considered. We updated plant family names to APG IV (*99*), averaged the proportion of taxa each family represented across the 72 plots and rank-ordered families that included 75% of tree species in 0.1-ha transects (Fig. 4A).

The family-level composition of leaves collected at each of the census sites (Table S5) of the Guaduas (Montecristo: 808 samples; 860017Ce: 842 samples), Bogotá (0903Ce: 1370 samples) and Cerrejón (0317Ce: 423 samples; 0705Ce: 767 samples) floras were compared with that of two modern Neotropical rainforests: the 50-hectare permanent plot at Barro Colorado Island (Panamá) (*37*) and the 25-hectare plot at Amacayacu (Colombia) (*38*). Taphonomic studies of leaves in tropical rainforests indicate that leaves retrieved from 0.5 x 0.5 m litter plots (~500 leaves) can represent up to 90% of the standing tree biomass in a 12.5 m radius (*36*). In order to best replicate these scenarios, quadrants of 22x22 m were selected within each plot in order to most closely approximate the area covered in a 12.5 m radius. Only trees with DBH>10 cm were considered for comparison with leaf census sites. Tree species accounting for the lowermost 10% cumulative biomass (estimated from DBH) were discarded and the remaining trees were used to estimate dissimilarity based on family abundance using Chao-Sørensen dissimilarity index (*100*). This index is a probabilistic approximation to the classic, presence/absence–based, Sørensen index used to assess compositional similarity between sites. The index incorporates species abundance information by weighing rare, shared species. As well as the classic Sørensen, this index ranges from 0 to 1, with 0 indicating the lowest dissimilarity (or highest similarity) and 1 indicating a maximum dissimilarity between sites.

One-hundred of these quadrants were randomly selected within the Amacayacu and BCI plots and were used to create a null distribution of dissimilarities within each plot and to estimate the average dissimilarity between living Neotropical rainforests and each of the leaf census sites (Fig. 4A). Autochthonous leaf assemblages reflect tree biomass as a combination of stem abundance and DBH. We used the relative number of trees in the plots to determine family abundance in extant sites, while for the fossil census sites we used the numbers of leaves for family abundance. All ferns were merged into a "fern" category, all conifers were integrated into a "conifer" category, and the gingers (Maranthaceae, Musaceae, Costaceae, Zingiberaceae and Cannaceae) were joined into "Zingiberales" due to the difficulty in identification among leaves of these families. We took a conservative approach and used natural affinities to establish family designations for the Paleocene floras and 'best guess' designations for the Maastrichtian sites. Despite the positive bias involved in using a 'best guess' family designation, the Maastrichtian census sites were more dissimilar to the forest plots than the Paleocene sites when resampling quadrants of 22x22m (BCI: Wilcoxon test, one-tailed, W=46882, $P<0.001$; Amacayacu: Wilcoxon test, one-tailed, W=7806, $P<0.001$), or of larger areas (Fig. S5). The Maastrichtian and Paleocene sites are equivalently dissimilar to extant sites when quadrants of 22x22m were selected; however, Maastrichtian and Paleocene sites are very different from each other in their dissimilarity to the extant sites (Table S11). All analyses were performed using R (*78*). Code and data files used in this analyses are available in Figshare digital repository, doi: 10.6084/m9.figshare.13611215.

Canopy structure

In closed-canopy forests, plant and soil respiration and the limited mixing of air between the understorey and the upper canopy creates a noticeable CO_2 enrichment inside the forest. This process results in the large range of $\delta^{13}C$ values seen in leaves of individual taxa living in closed-

canopy, multistratal forests (*40*). Canopy structure is also reflected in the leaf anatomy of living trees. Vein length per area (VLA) measured in leaves of individual tree taxa shows a bimodal distribution in response to the vertical gradient of light created by multiple light-intercepting leaf strata in closed-canopy forests (*39*). Graham et al. (*40*) and Crifo et al. (*39*) used leaf cuticles and measurements of vein length per area, respectively, to test for a closed-canopy structure in the Guaduas and Cerrejón floras.

It was not possible to replicate these analyses for the Bogotá flora, as no leaf cuticles have yet been collected from the Bogotá Formation and the highest order venation is not well-preserved in these leaf impressions. Therefore, changes in canopy structure across the Maastrichtian-Paleocene interval are inferred based on the Guaduas and Cerrejón floras only.

Insect Damage

Insect damage was quantified and compared from sites representing single time slices having samples with collections of more than 400 leaves (Data S6; Figshare digital repository, doi: 10.6084/m9.figshare.13611215). Presence-absence of standardized insect-feeding damage types (DTs) were scored on 659 complete or nearly complete leaves of non-monocot (ANA-grade, magnoliids and eudicots) angiosperms of the Montecristo site of the Guaduas flora, and 871 leaves of the Checua (422 leaves) and Cogua (449 leaves) sites of the Bogotá flora, following the *Guide to Insect (and Other) Damage Types on Compressed Plant Fossils* (*101*) and subsequent updates. Six new damage types (Fig. S6) from the Guaduas and Bogotá floras are described in the Supplementary text and will be further documented and illustrated, with their modern analogs, in the Version 4 of the *Guide to Insect (and Other) Damage Types on Compressed Plant Fossils*. Insect damage from 507 leaves from the Cerrejón flora (*19*) was also included in these analyses. DTs were assigned a score of 1, 2 or 3 of increasing specificity based on observations of modern ecological analogs (*101*). Values of 1 were assigned to generalized damage made by insects feeding on numerous unrelated hosts, and value of 3 were assigned to highly specialized damage caused by insects feeding on one or a few closely related host species. In our analyses, we considered specialized DTs to be those with values of 2 or 3. When possible, DTs inflicted by leaf miners were considered separately because of their high host-specificity.

Resampling curves for total, specialized and leaf miner DT richness at each site (Fig. S7) were estimated using "vegan" (*84*). Insect damage richness and frequency were compared across the Guaduas, Bogotá and Cerrejón floras. Total and specialized DT frequency was estimated at each site as the percentage of damaged leaves in 400 specimens randomly sampled without replacement and averaged over resampling 100 iterations. Total and specialized DT richness was calculated at 95% sample coverage using the package "iNEXT" (*102*) and differences in richness were assessed via t-tests using R (*78*). The average number of DTs per host at each site was quantified using leaf morphotypes having more than 20 specimens. The total numbers of DTs observed on each host were used to estimate an overall site mean (Fig. S8). Morphotypes having more than 20 specimens (Guaduas: 11 morphotypes; Bogotá: 8 morphotypes; Cerrejón: 8 morphotypes; Fig. S8) were also used for quantifying leaf damage turnover across host pairs as a means to assess herbivore specificity within each site. Turnover across host pairs was calculated using the Chao-Sørensen dissimilarity index (*100*) and was based on the mean vectors of insect-feeding DTs found in 20 randomly selected leaves from each host, averaged over 1000 resampling iterations. A null expectation for this comparison assumes that DTs are equally distributed across morphotypes and that their probability of occurrence on any given leaf follows the relative abundance of DTs in each flora. We created a distribution for dissimilarities under

this null expectation: four hundred randomly selected leaves were selected from each site and the observed relative abundance of each DT was used to establish a probability of occurrence on any given leaf and any given host. Pairwise dissimilarities expected under this null hypothesis were computed from 20 leaves per host and resampled over 1000 iterations, considering that DT distribution was the same across all hosts. The distribution of observed dissimilarities across host pairs were compared to this null expectation at each site using a Wilcox-test implemented in R (*78*). Code is available in Figshare digital repository, doi: 10.6084/m9.figshare.13611215.

Supplementary Text

LA-ICPMS methods

Zircon grains were separated from sample D-928 (*89*) using standard techniques and imaged with cathodoluminescence (CL) using a JEOL JSM-1300 scanning electron microscope and Gatan MiniCL. Zircon was analyzed by LA-ICPMS using a ThermoElectron X-Series II quadrupole ICPMS and New Wave Research UP-213 Nd:YAG UV (213 nm) laser ablation system. In-house analytical protocols, standard materials, and data reduction software were used for acquisition and calibration of U-Pb dates and a suite of high field strength elements (HFSE) and rare earth elements (REE). Zircon was ablated with a laser spot of 30 μm wide using fluence and pulse rates of 5 J/cm^2 and 10 Hz, respectively, during a 45 second analysis (15 sec gas blank, 30 sec ablation) that excavated a pit ~25 μm deep. Ablated material was carried by a 1.2 L/min He gas stream to the nebulizer flow of the plasma. Dwell times were 5 ms for Si and Zr, 200 ms for ^{49}Ti and ^{207}Pb, 80 ms for ^{206}Pb and ^{238}U, 40 ms for ^{202}Hg, ^{204}Pb, ^{208}Pb, ^{232}Th and 10 ms for all other HFSE and REE. Background count rates for each analyte were obtained prior to each spot analysis and subtracted from the raw count rate for each analyte. Ablations pits that appeared to have intersected glass or mineral inclusions were identified by time-resolved data that show large fluctuations in Ti or P. U-Pb dates from these analyses are considered valid if the time-resolved U-Pb ratios appear to have been unaffected by the inclusions. Analyses that appeared contaminated by common Pb were rejected based on an intensity of mass 204 above baseline. For concentration calculations, background-subtracted count rates for each analyte were internally normalized to ^{29}Si and calibrated with respect to NIST SRM-610 and -612 glasses as the primary standards. Temperature was calculated from the Ti-in-zircon thermometer. Because there are no constraints on the activity of TiO_2 in the source rocks, an average value in crustal rocks of 0.6 was used.

For U-Pb and ^{207}Pb/^{206}Pb dates, instrumental fractionation of the background-subtracted ratios was corrected and dates were calibrated with respect to interspersed measurements of the Plesovice zircon standard (*103*). Two analyses of Plesovice were done for every 10 analyses of unknown zircon; a polynomial fit to the standard analyses yields each sample-specific fractionation factor. Signals at mass 204 were indistinguishable from zero following subtraction of mercury backgrounds measured during the gas blank (<1000 cps ^{202}Hg), and thus dates are reported without common Pb correction. Radiogenic isotope ratio and age error propagation for all analyses includes uncertainty contributions from counting statistics and background subtraction. For spot analyses that are individually interpreted (e.g., detrital zircon analyses), the uncertainty from the standard calibration is propagated into the error on each date. This uncertainty is the standard deviation of the time-varying U/Pb fractionation factor and the standard error of the mean of the time-invariant, smaller ^{207}Pb/^{206}Pb fractionation factor. For groups of analyses that are collectively interpreted from a weighted mean date, a weighted mean date is first calculated using Isoplot 3.0 (*104*) using errors on individual dates that do not include

the standard calibration uncertainties, and then the standard calibration uncertainty is propagated into the error on the weighted mean date. Standard calibration uncertainties for $^{207}Pb/^{206}Pb$ and $^{206}Pb/^{238}U$ dates are 0.3% and 1.9% (2σ). Age interpretations are based on $^{206}Pb/^{238}U$ dates. Errors on the dates from individual analyses are given at 2σ, as are the errors on the weighted mean dates. Two zircon secondary reference materials were treated as unknowns to assess accuracy, interspersed as groups of two analyses for every 20 unknown analyses. Weighted mean dates are calculated using Isoplot 3.0 (*104*) from errors on individual dates that do not include the standard calibration uncertainties. However, errors on weighted mean dates include the standard calibration uncertainties within each experiment and are given at 2σ. AUSZ2 zircon (38.9 Ma from unpublished chemical abrasion thermal ionization mass spectrometry (CA-TIMS) data, Boise State University) yielded a weighted mean $^{206}Pb/^{238}U$ date of 39.4 ± 0.7 Ma (MSWD=1.3, n=8). OG1 zircon (3465 Ma from unpublished CA-TIMS data, Boise State University) yielded a weighted mean $^{206}Pb/^{238}U$ date of 3475 ± 32 Ma (MSWD=1.1, n=10). These results show that accurate $^{206}Pb/^{238}U$ dates were obtained.

Fifty-one grains from sample D-928 analysed by LA-ICPMS yielded $^{206}Pb/^{238}U$ dates from 245 ± 17 to 53 ± 5 Ma (errors include standard calibration uncertainty). The major age peak is at ~60 Ma, and minor peaks are at ~85, 150, and 245 Ma. The dates between 65 and 53 Ma were uniformly dispersed. Seven grains were selected for CA-TIMS dating from the grains that yielded LA-ICPMS dates between 61 and 53 Ma, considering their chemistry. Five grains were selected from the majority of grains from a chemically similar group, and two grains were selected from the minority of grains that formed another chemically similar group.

CA-TIMS Methods

Single zircon grains were removed from the epoxy mounts and subjected to a modified version of the chemical abrasion method of Mattinson (*105*), reflecting analysis of single grains. Grains were placed in a muffle furnace at 900°C for 60 hours in quartz beakers, transferred to 3 ml Teflon PFA beakers and loaded into 300 µl Teflon PFA microcapsules. Fifteen microcapsules were placed in a large-capacity Parr vessel, and the crystals partially dissolved in 120 µl of 29 M HF for 12 hours at 180°C. The contents of each microcapsule were returned to 3 ml Teflon PFA beakers, the HF removed and the residual grains immersed in 3.5 M HNO_3, ultrasonically cleaned for an hour, and fluxed on a hotplate at 80°C for an hour. The HNO_3 was removed and the grains were rinsed twice in ultrapure H_2O before being reloaded into the same 300 µl Teflon PFA microcapsules (rinsed and fluxed in 6 M HCl during crystal sonication and washing) and spiked with the EARTHTIME mixed ^{233}U-^{235}U-^{205}Pb tracer solution (ET535). These chemically abraded grains were dissolved in Parr vessels in 120 µl of 29 M HF with a trace of 3.5 M HNO_3 at 220°C for 48 hours, dried to fluorides, and then re-dissolved in 6 M HCl at 180°C overnight. U and Pb were separated from the zircon matrix using an HCl-based anion-exchange chromatographic procedure (*106*), eluted together and dried with 2 µl of 0.05 N H_3PO_4. Pb and U were loaded on a single outgassed Re filament in 5 µl of a silica-gel/phosphoric acid mixture (*107*), and U and Pb isotopic measurements made on a GV Isoprobe-T multicollector thermal ionization mass spectrometer equipped with an ion-counting Daly detector. Pb isotopes were measured by peak-jumping all isotopes on the Daly detector for 160 cycles. Pb mass fractionation was corrected using the known $^{202}Pb/^{205}Pb$ ratio of the ET2535 tracer solution that was recently measured on other samples. Transitory isobaric interferences due to high-molecular weight organics, particularly on ^{204}Pb and ^{207}Pb, disappeared within approximately 30 cycles, while ionization efficiency averaged 10^4 cps/pg of each Pb isotope. Linearity (to ≥1.4 x 10^6 cps)

and the associated deadtime correction of the Daly detector were monitored by repeated analyses of NBS982, and have been constant since installation. Uranium was analyzed as UO_2^+ ions in static Faraday mode on 10^{11} ohm resistors for 250 cycles, and corrected for isobaric interference of $^{233}U^{18}O^{16}O$ on $^{235}U^{16}O^{16}O$ with an $^{18}O/^{16}O$ of 0.00206. Ionization efficiency averaged 20 mV/ng of each U isotope. U mass fractionation was corrected using the known $^{233}U/^{235}U$ ratio of the ET535 tracer solution. CA-TIMS U-Pb dates and uncertainties were calculated using the algorithms of Schmitz and Schoene (*108*), ET535 tracer solution (*109*, *110*) with calibration of $^{235}U/^{205}Pb$ = 100.233, $^{233}U/^{235}U$ = 0.99506, and $^{205}Pb/^{204}Pb$ = 11268, and U decay constants recommended by Jaffey et al. (*111*). $^{206}Pb/^{238}U$ ratios and dates were corrected for initial ^{230}Th disequilibrium using a Th/U[magma] = 3.0 ± 0.3 using the algorithms of Crowley et al. (*112*), resulting in an increase in the $^{206}Pb/^{238}U$ dates of ~0.09 Ma. All common Pb in analyses was attributed to laboratory blank and subtracted based on the measured laboratory Pb isotopic composition and associated uncertainty. U blanks are difficult to precisely measure, but are estimated at 0.075 pg. A weighted mean $^{206}Pb/^{238}U$ date was calculated from equivalent dates using Isoplot 3.0 (*104*). Error on the weighted mean $^{206}Pb/^{238}U$ date is the internal error based on analytical uncertainties only, including counting statistics, subtraction of tracer solution, and blank and initial common Pb subtraction. It is given at the 2 sigma confidence interval. This error should be considered when comparing our date with $^{206}Pb/^{238}U$ dates from other laboratories that used the same EARTHTIME tracer solution or a tracer solution that was cross-calibrated using EARTHTIME gravimetric standards. When comparing our date with those derived from laboratories that did not use the same EARTHTIME tracer solution or a tracer solution that was cross-calibrated using EARTHTIME gravimetric standards, a systematic uncertainty in the tracer calibration of 0.05% should be added to the internal error in quadrature. This error is ± 0.04 Ma. When comparing our date with those derived from other decay schemes (e.g., $^{40}Ar/^{39}Ar$, ^{187}Re-^{187}Os), systematic uncertainties in the tracer calibration and ^{238}U decay constant (*111*) should be added to the internal error in quadrature. This error is ± 0.07 Ma. Errors on the $^{206}Pb/^{238}U$ dates from individual grains are also given at the 2 sigma confidence interval.

The CA-TIMS $^{206}Pb/^{238}U$ yielded dates from 60.87 ± 0.04 to 60.71 ± 0.04 Ma (Data S2). The five dates that exclude the oldest and youngest analyses are equivalent with a weighted mean of 60.79 ± 0.02 Ma (MSWD = 0.9). Because it cannot be ruled out that all analyzed grains are detrital rather than primary volcanic, the age of the volcanic ash at meter 928 is best interpreted as 60.79 ± 0.02 Ma or younger.

New Damage Types

Six new damage types (DTs) were established in this study: DT359, DT360, DT361 and DT362 from the Guaduas Formation of Colombia, and DT364 and DT365 from the Bogotá Formation of Colombia. These DTs will be further documented and illustrated, with their modern analogs, in the Version 4 of the *Guide to Insect (and Other) Damage Types on Compressed Plant Fossils*.

New Damage Type DT359

Figured specimen. STRI-19053 (Fig. S6A–B)

Description. An isolated, hemispheroidal, foliar gall, avoiding major and minor veins, circular in outline and approximately 1 mm in diameter; the mature gall has a surface that is ornamented by subtle pustules and smooth, and is preserved as a charcoalified crust; the central chamber is spheroidal, eccentrically placed and barely detectible; the nutritive tissue zone cannot be distinguished; the outer wall is very thin, lacks a defined rim, but its surface is exposed with

scattered, ovoidal to elliptical pustules about 0.05 mm in diameter and length, separated by smooth inter-areas. [Blister gall]
Functional feeding group. Galling.
Host specificity. 1.
Feeding event data. Single occurrence.
Host plant. GD32 (aff. Theaceae).
Locality. Ubaté, Boyacá Province, Colombia.
Stratigraphy. Guaduas Formation.
Age. Cretaceous Period, Maastrichtian Stage.
Specimen. STRI-19053.
Repository. Museo Paleontológico Royo-y-Gómez, Servicio Geológico Colombiano, Bogotá, Colombia.
Inferred culprit. Diptera, Cecidomyiidae (gall midge).
Other material. STRI-18468, STRI-18475, STRI-18597, STRI-18670, STRI-18697, STRI-18700, STRI-18709, STRI-18788, STRI-18800, STRI-18808, STRI-19023, STRI-19040, STRI-19230, STRI-19250, STRI-19272, STRI-19288, STRI-19300, STRI-19310, STRI-19351, STRI-19361, STRI-19991, STRI-20521, STRI-20712.
Remarks. This type of hemispheroidal, rather thick, blister gall is commonly produced by gall midges. A common modern analog would be the gall produced by *Dasineura*, which has a very wide host preference on both herbaceous and woody hosts and is particularly prominent among Rosaceae.

New Damage Type DT360
Figured specimen. STRI-19128(Fig. S6C–D)
Description. Isolated occurrence of a medium size, circular to broadly ovate scale impression mark present on foliage but not associated with significant veins; the marks are preserved without organic covers but have a finely granulose surface on which are 10 to 15 round pustules that are from 0.1 to 0.3 mm in diameter, and the marks are about 3.5 mm by 4 mm in dimensions; the distinctive scale-impression marks do not occur in clusters and are solitary occurrences on leaf surfaces. [Scale insect-covering damage]
Functional feeding group. Piercing and sucking.
Host specificity. 3.
Feeding event data. Single occurrence.
Host plant. GD35 (Lauraceae)
Locality. Ubaté, Boyacá Province, Colombia.
Stratigraphy. Guaduas Formation.
Age. Cretaceous Period, Maastrichtian Stage.
Specimen. STRI-19128.
Repository. Museo Paleontológico Royo-y-Gómez, Servicio Geológico Colombiano, Bogotá, Colombia.
Inferred culprit. Hemiptera, Sternorrhyncha, Diaspididae (armored scale insect).

Other material. STRI-18360, STRI-18648, STRI-19042, STRI-19068, STRI-19110, STRI-19127, STRI-19244.
Remarks. This type of scale insect is similar to the covers of modern sweetgum scale on *Liquidambar styraciflua* from the Southeastern United States. The pustules on the cover of the fossil, however, are positioned differently than that of its modern analog.

New Damage Type DT361
Figured specimen. STRI-19128 (Fig. S6C, S6E)
Description. A compound gall consisting of a loose, circular cluster of 8 to 20, small, spheroidal to ellipsoidal galls occurring adjacent to and often touching each other and positioned on foliage surfaces without regard to underlying veins; the mature gall is 0.2 mm to 0.4 mm in diameter, bears a single, rounded ovoidal, ellipsoidal or reniform chamber, which is encompassed by a modest nutritive tissue zone, and in turn is surrounded by outer walls that are thick, lightly-hued and spinose; each chamber of this gall apparently is well defended by thick and spinose outer walls. [Blister or bladder gall]
Functional feeding group. Galling.
Host specificity. 2
Feeding event data. Single (bulk) occurrence.
Host plant. GD35 (Lauraceae)
Locality. Ubaté, Boyacá Province, Colombia
Stratigraphy. Guaduas Formation
Age. Cretaceous Period, Maastrichtian Stage.
Specimen. STRI-19128.
Repository. Museo Paleontológico Royo-y-Gómez, Servicio Geológico Colombiano, Bogotá, Colombia
Inferred culprit. Trombidiformes: Eriophyidae (gall mite).
Other material. STRI-18635, STRI-18636, STRI-18638, STRI-18639, STRI-18640, STRI-18643, STRI-19110, STRI-19218, STRI-20388.
Remarks. This is a compound gall that is typical of gall mites. Each of the 18, small, encapsulated galls contain an individual galler that is walled off by a thick wall. The limits of the compound gall are circumscribed by the faint encircling border separating the inner altered tissue from the surrounding tissue that displays very fine venation.

New Damage Type DT362
Figured specimen. STRI-19246 (Fig. S6F)
Description. A semicircular, excised leaf fragment that retains a portion of a normal, unaltered leaf margin on one side and shows a convex, semicircular cut margin with callus or other reaction tissue and up to 180^0 of inscribed arc on the other side; chord length from 4 mm to 10 mm, with truncated veins present; the excisions are complementary to and precisely match in outline the neat-exact semicircularity of DT81; the excision is the source of the leaf. [Leafcutter bee damage]

Functional feeding group. Margin feeding.
Host specificity. 3.
Feeding event data. Single occurrence.
Host plant. GD52 (aff. Urticaceae).
Locality. Ubaté, Boyacá Province, Colombia.
Stratigraphy. Guaduas Formation.
Age. Cretaceous Period, Maastrichtian Stage.
Specimen. STRI-19246.
Repository. Museo Paleontológico Royo-y-Gómez, Servicio Geológico Colombiano, Bogotá, Colombia.
Inferred culprit. Hymenoptera: Megachilidae (leafcutter bee).
Other material.
Remarks. This segment of a leaf edge with arcuate, incised margins are the result of a leafcutter bee, or less likely leafcutter ant, that excises leaf discs or partial leaf discs from the edges of leaves. DT362, consequently, would be the complement pieces to DT81. These discs likely were accidentally dropped by a leafcutter bee before it was to be incorporated into a nest with leafcutter bee larvae.

New Damage Type DT364
Figured specimen. STRI-12349 (Fig. S6G)
Description. Cylindrically shaped case-bearer structures lying prostrate along a leaf surface with evidence of adjacent leaf mining; the mines are circular to broadly ellipsoidal scars slightly less than 1 mm in maximum dimension; the cases have a finely opaque surface, one open end, are 1 mm wide by up to 5 mm long, oriented adjacent and parallel to the leaf margin, and preserved as compressions on the leaf surface of two adjacent leaves belonging to the same host-plant species; these cases are significantly different in structure than DT131, the other leaf-mining case bearer. [Case-bearer damage]
Functional feeding group. Mining.
Host specificity. 3
Feeding event data. Single occurrence.
Host plant. BF38 (Fabaceae)
Locality. Nemocón, Cundinamarca Province, Colombia.
Stratigraphy. Bogotá Formation.
Age. Paleogene Period, Selandian–Thanetian Stage.
Specimen: STRI-12349.
Repository. Museo Paleontológico Royo-y-Gómez, Servicio Geológico Colombiano, Bogotá, Colombia.
Inferred culprit. Lepidoptera: Coleophoridae (casebearing moths)
Other material. STRI-12367, STRI-12378, STRI-12416.
Remarks. Along the margin of the leaf is preserved the external cases of a leaf-mining casebearer moth. These micromoths construct a silken case for the larva and attach the head and mouthparts

to the plant surface, penetrating the inner tissues as they mine the adjacent inner tissues of the host. The casebearer typically leaves a circular patch of damage that is approximately the same diameter as the case.

New Damage Type DT365
Figured specimen. STRI-12328. (Fig. S6H)
Description. A pattern of irregular, linear, often subparallel swaths of removed surface tissue approximately coursing along the leaf edge or adjacent its midrib; each swath 0.6 to 0.9 mm wide, bounded by two, prominent, parallel reaction rims that are mostly undulose and parallel to one another, containing wispy, dark, thread-like extensions into the inner abraded area; present throughout the leaf but frequently avoiding the elongate area along the midway between the midrib and margin.
Functional feeding group. Surface feeding.
Host specificity. 2
Feeding event data. Pattern occurrence.
Host plant. BF21 (Fabaceae)
Locality. Cogua, Cundinamarca Province, Colombia.
Stratigraphy. Bogotá Formation.
Age. Paleogene Period, Selandian–Thanetian Stage.
Figured specimen. STRI-12328
Repository. Museo Paleontológico Royo-y-Gómez, Servicio Geológico Colombiano, Bogotá, Colombia.
Inferred culprit. Lepidoptera: Noctuidae (cutworm).
Other material. STRI-12414.
Remarks. The best match for this type of damage is that made by a variety of lepidopteran leaf skeletonizers, such as cutworms. However, DT365 is not particularly distinctive, and could have been made, although less likely, by caterpillars and externally feeding larvae belonging to a variety of lepidopteran, hymenopteran and coleopteran lineages.

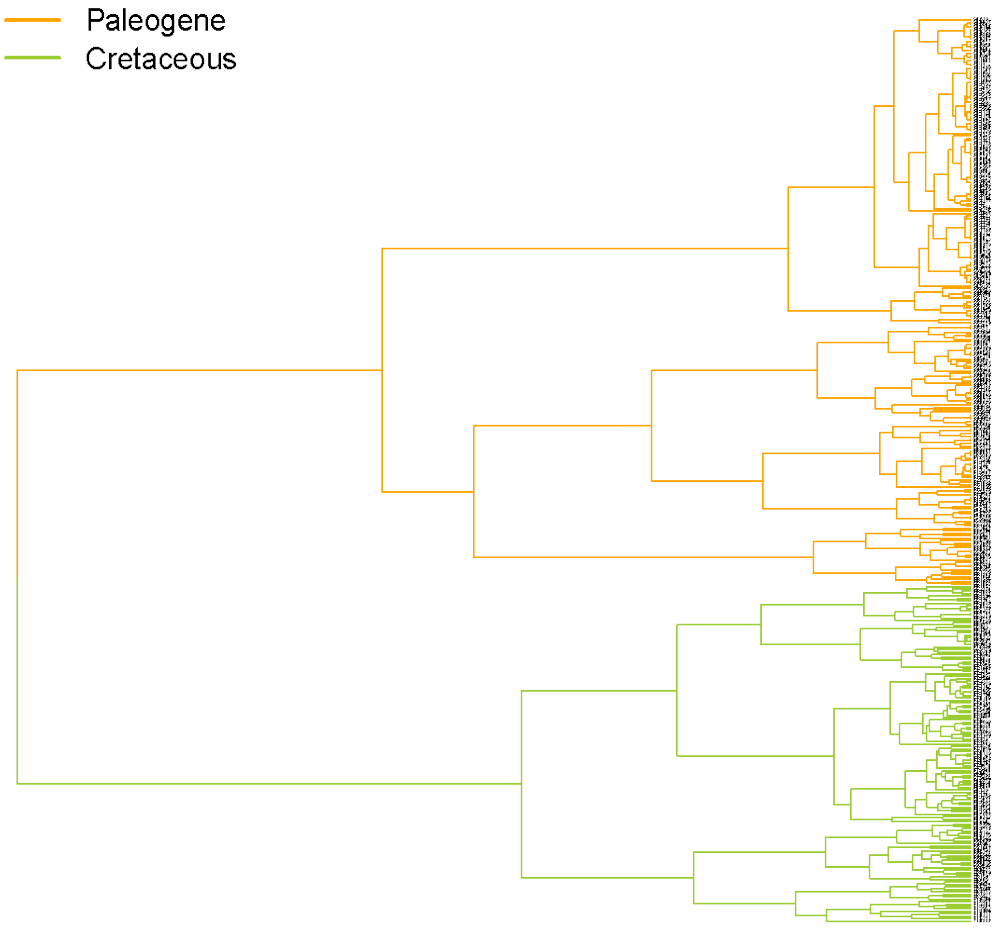

Fig. S1.
Cluster analysis based on community composition of palynofloras from individual samples spanning the Maastrichtian–Paleocene interval.

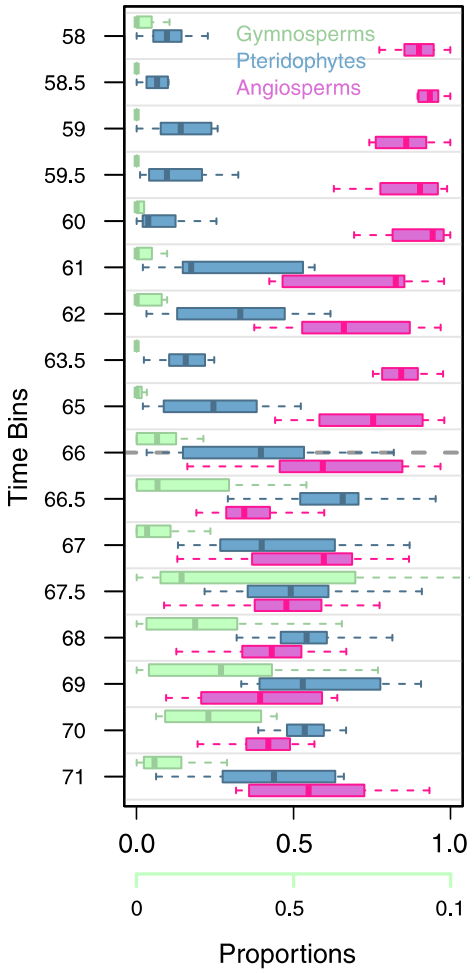

Fig. S2.
Change in proportions of the three broad taxonomic categories of palynomorphs across the Maastrichtian–Paleocene interval.

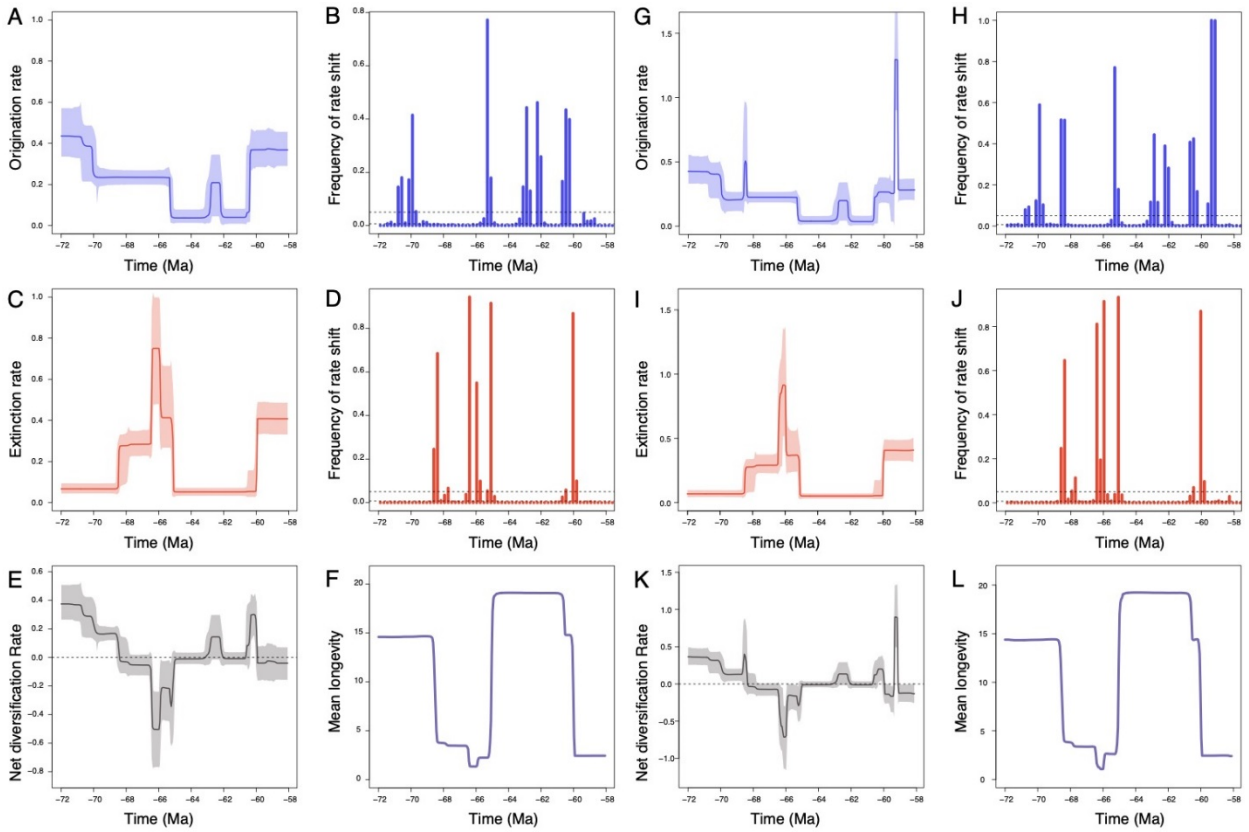

Fig. S3.
Posterior estimates of origination and extinction rates through time as inferred by PyRate using reversible jump Markov Chain Monte Carlo. Marginal estimates of origination rates (A) and extinction rates (C) through time are shown as mean and 95% credible intervals (shaded areas). The frequency of a sampled rate shift is computed within small time bins for origination and extinction rates (B and D, respectively), with dashed lines indicating log-Bayes factors of 6. Sampling frequencies higher that the dashed line indicate strong statistical support for a rate shift. Plot (F) shows net diversification rates through time (computed as the posterior difference between origination and extinction rates through time) and estimated mean taxon longevity (estimated as the inverse of the extinction rate). Panels G–L show the result of a re-analysis of the data after allowing for a higher temporal resolution in the RJMCMC search algorithm, i.e. setting the minimum allowed distance between rate shifts to 0.2 Myr (note that the Y-axis scale is different from that in A–F). While the inferred extinction dynamics were negligibly different from the ones obtained under a coarser time resolution (I), origination rates showed brief peaks (H) otherwise undetected in the coarser analysis. Most notably, this analysis recovered an additional short but strong increase in origination rates between 59.6 and 59.2 Ma.

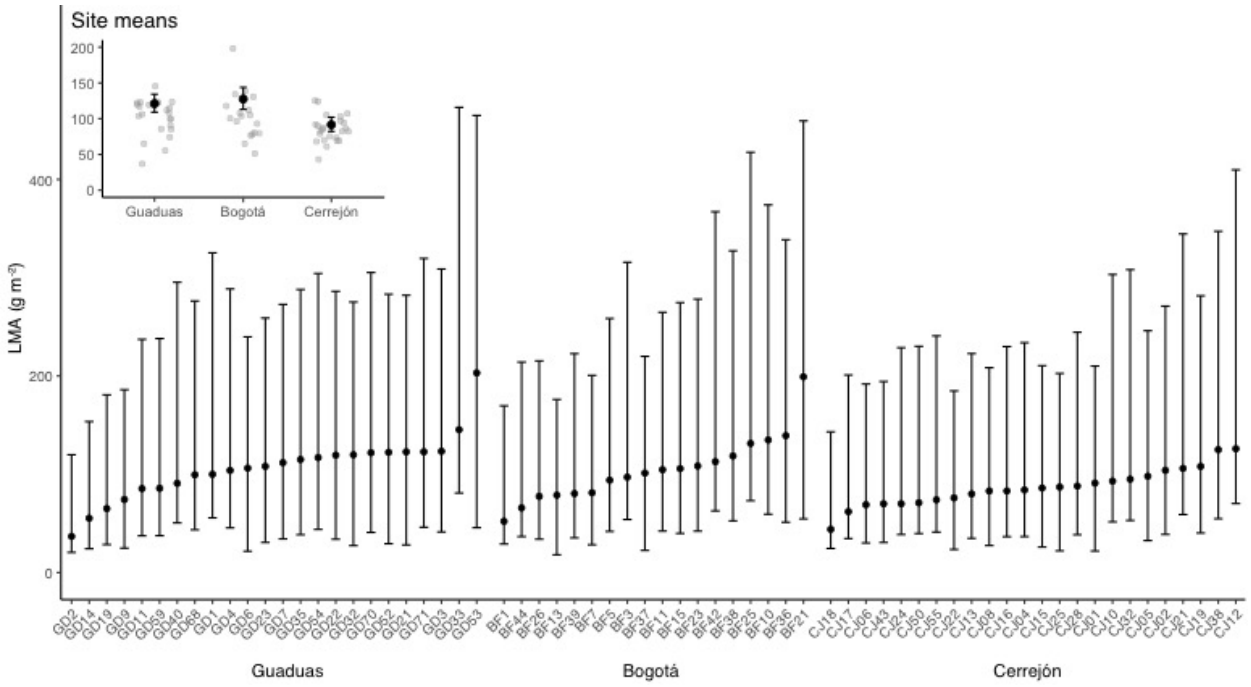

Fig. S4.
Leaf mass per area (LMA) in the Guaduas (Maastrichtian), Bogotá (Paleocene) and Cerrejón (Paleocene) floras. LMA for leaf morphotypes estimated based on (*30*). Black lines represent 95% prediction intervals. Top left insert depicts LMA means per flora (black dots) and 95% prediction intervals (black lines). Gray points represent estimates for individual leaf morphotypes.

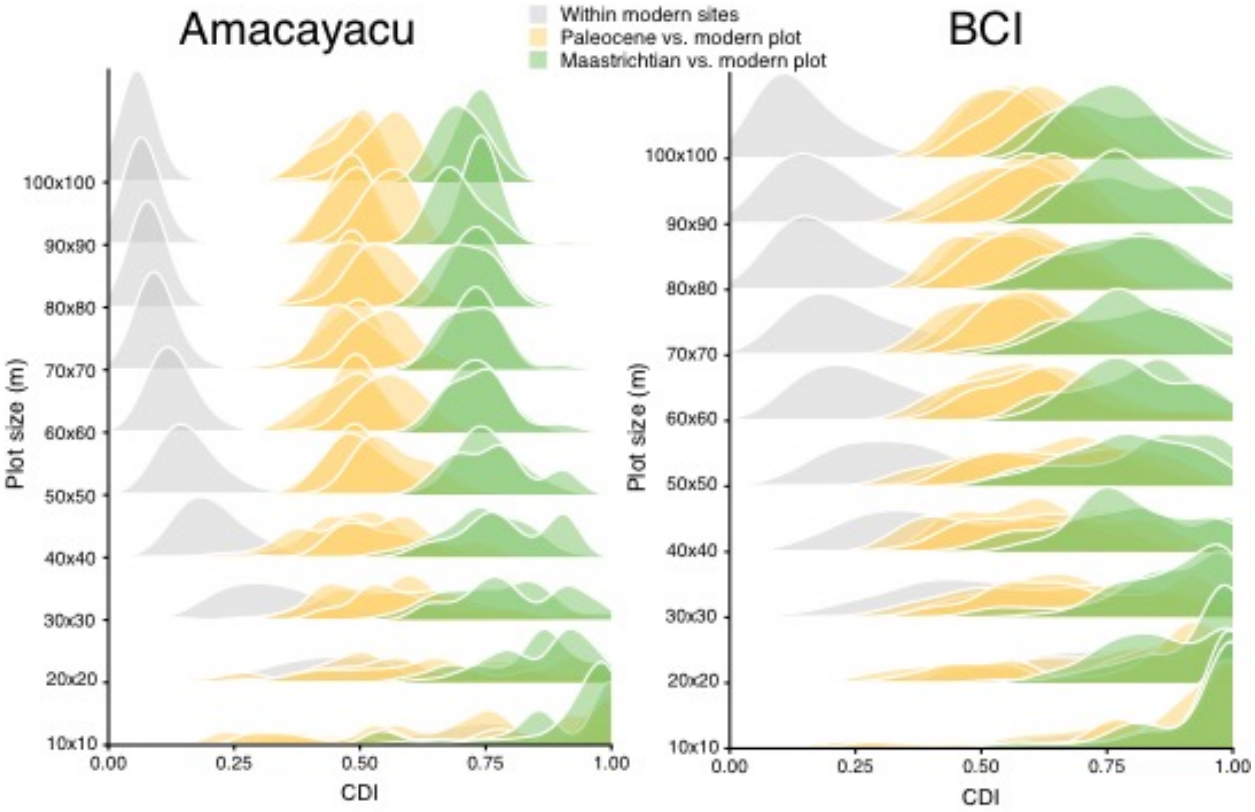

Fig. S5.
Density plots for dissimilarity (Chao-Sorensen Dissimilarity index, CDI) at the family-level, estimated between leaves from unbiased fossil census sites and trees found in 50 randomly selected areas of varying size within the 25-ha permanent forest plot at Amacayacu (Colombia) and the 50-ha permanent forest plot at Barro Colorado Island (Panama).

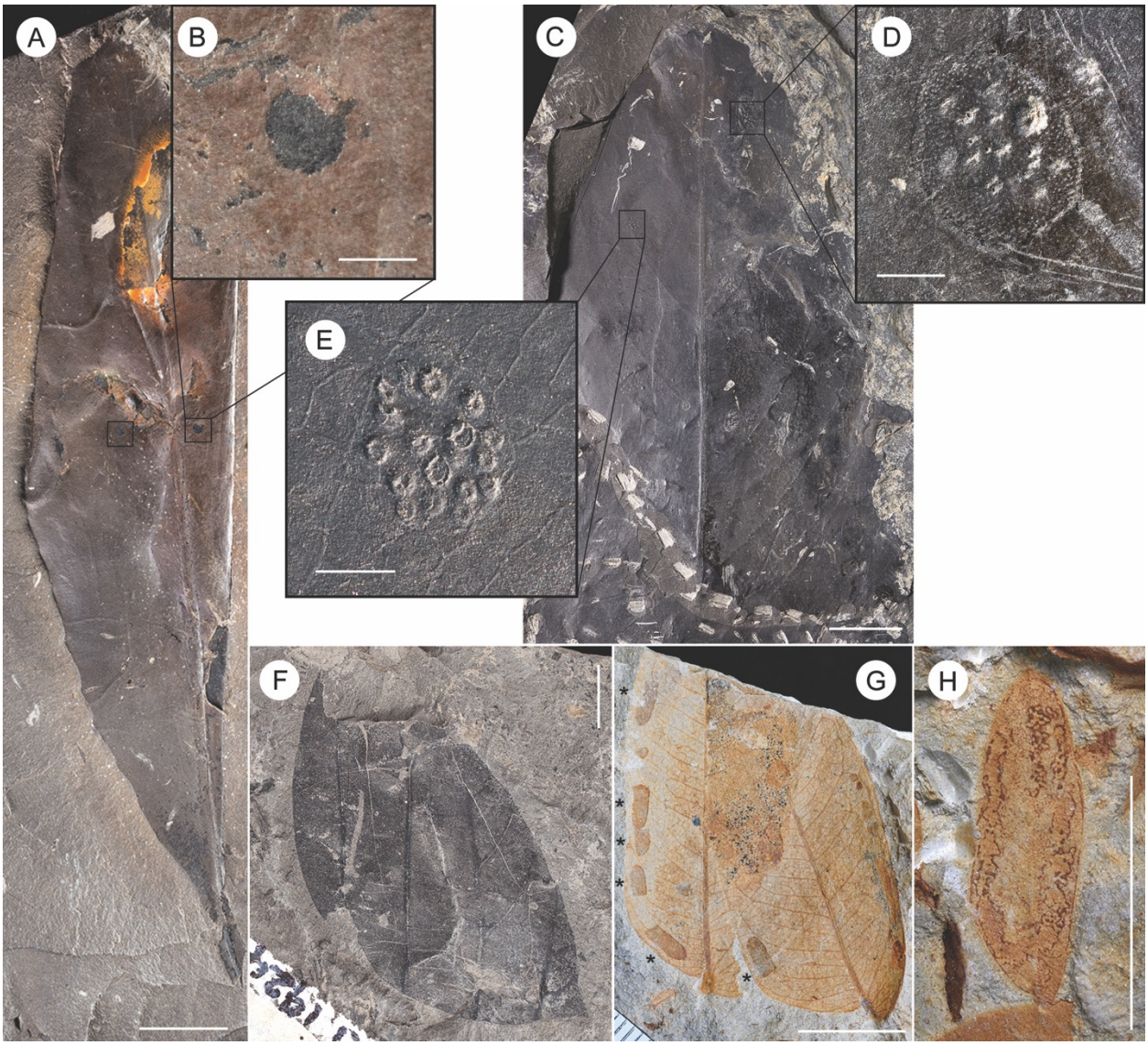

Fig. S6.
New damage types described from the Guaduas (A–F) and Bogotá (G–H) floras. (A) GD32 (STRI-19053; aff. Theaceae) bearing two foliar galls DT359. Scale bar =1cm. (B) Close-up of (A) showing detail of DT359. Scale bar =1mm. (C) GD35 (STRI 19128; aff. Lauraceae) bearing scale impression DT360 and oviposition DT361. Scale =1cm. (D) Detail of circular to broadly ovate scale impression DT360. Scale bar =1mm. (E) Detail of compound gall DT361, showing a loose, circular cluster of 8 to 20, small, spheroidal to ellipsoidal galls. Scale bar =1mm. (F) Margin feeding DT362 on GD52 (STRI 19246; aff. Urticaceae), consisting of a semicircular, excised leaf fragment that retains a portion of the leaf margin. Scale bar =1cm. (G) DT364 on BF32 (STRI 12349; Fabaceae), showing cylindrically shaped case-bearer structures (asterisks) lying prostrate along a leaf surface with evidence of adjacent leaf mining. Scale bar = 1cm. (H) DT365 on BF21 (STRI 12328; Fabaceae), showing a pattern of irregular swaths of removed surface tissue approximately coursing along the leaf edge. Scale bar =5mm.

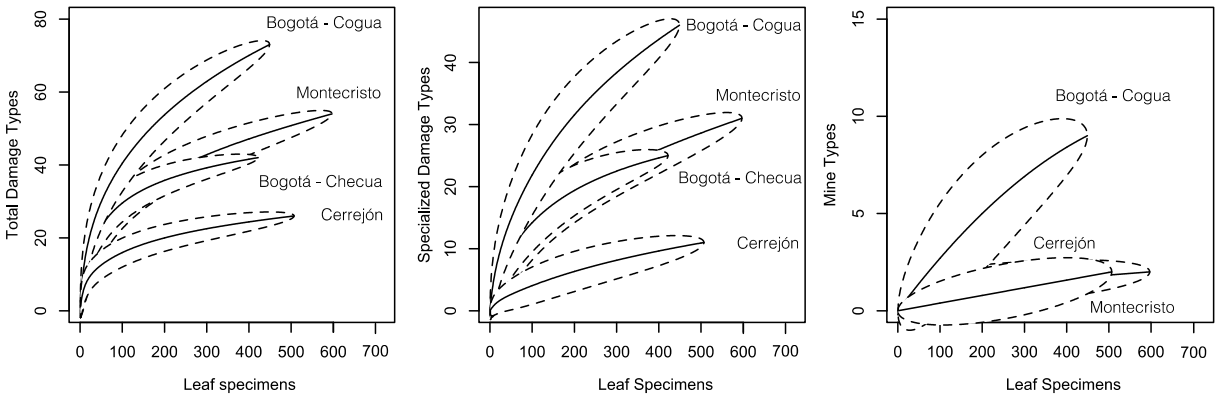

Fig. S7.
Resampled insect-damage richness on the Maastrichtian Guaduas (Montecristo) and Paleocene Bogotá (Checua, Cogua) and Cerrejón. (A) Total insect damage. (B) Specialized insect damage. (C) Leaf miners. Dotted lines indicate ±1σ.

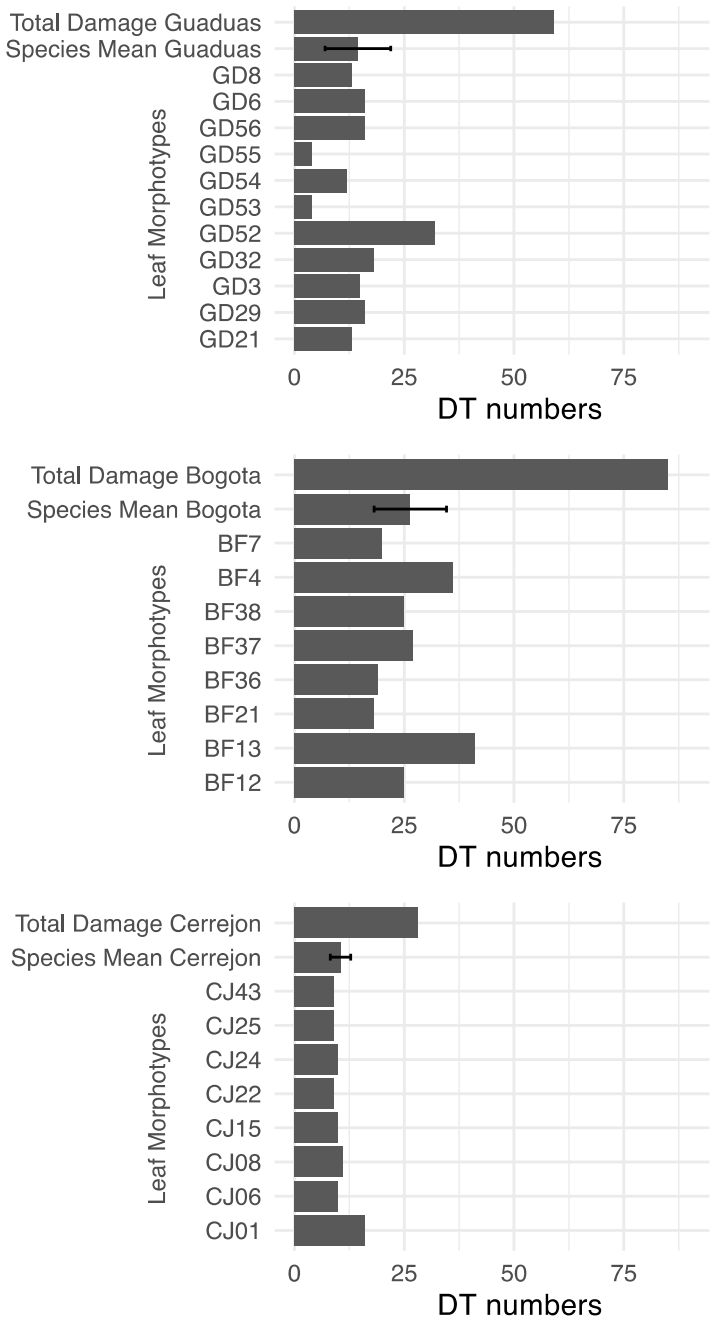

Fig. S8.
Raw numbers of DTs per site and for leaf morphotypes having >20 leaves. Black bars indicate ±1σ.

Table S1.
Localities of the studied sections spanning the Maastrichtian-Paleocene interval.

SiteCode	Lat	Lon	Type
A1	6.95	-71.86	Well
A2	6.57	-71.5	Well
A3	6.59	-71.49	Well
A4	6.98	-71.84	Well
B3	4.98	-72.75	Well
B15	4.57	-72.43	Well
CS1	6.45	-73.34	Well
CD	11.1	-72.69	Well
CG3	8.12	-72.44	Well
CS	4.84	-73.22	Outcrop
CP1	4.26	-73.11	Well
DK	3.05	-75.17	Well
F3	5.29	-72.25	Well
F	2.95	-75.07	Outcrop
GI	7.04	-72.18	Well
G1	2.16	-75.33	Well
GO1	8.27	-72.58	Well
G	6.56	-73.71	Well
GU1	4.74	-73.14	Well
GU2	4.42	-73.09	Well
J	6.99	-71.53	Well
L3	9.57	-73.35	Well
LM1	5.04	-72.31	Well
LE1	7.06	-73.32	Well
M	4.5	-73.1	Outcrop
M3	8.06	-72.31	Well
P1	3	-75.16	Well
RG	7.4	-72.4	Outcrop
R1	6.53	-73.33	Well
R14	9.1	-72.9	Well
RL	8.4	-71.8	Outcrop
RC1	4.93	-72.73	Well
R	5.37	-73.17	Well
T2	6.34	-71.45	Well
TS	5.13	-73.5	Outcrop
T182	8.59	-72.67	Well
U	7.25	-73.37	Outcrop
V2	9.81	-73.59	Well
Z1	8.12	-72.27	Well

Table S2.
Additional Calibration points to Jaramillo et al. (*68*) Palynological Zonation.

Datum	Composite Unit	Age (Ma)
Iridium anomaly (*113*)	19842	66
FAD *Micula prinsii*	19886	67.2
FAD *Abathom. mayaroensis*	19941	68.72
FAD *Gansserina gansseri*	20008.5	72.35
FAD *Globotruncana aegyptiaca*	20600	73.27
LAD *Eiffellithus eximius*	21000	75.87
Ammonites (*114*)	21640	83.6

Table S3.
Time-bins attributes. Tbin = Time bin; P = Period (Maastrichtian [M], Paleogene[Pg]); NS = number of samples include n the bin; Occs = Number of total grains (occurrences); Tsp = Time span of bins (My); Locs = Number of localities represented in each bin; Area = total area (km^2) of the minimum polygon that included all localities represented on each bin (package "geosphere";(*88*); Rich = richness (*20*), Ext = Extinction and Ori = origination rates (*22*), U = coverage of diversity estimator, and Chao index. Numbers in parenthesis indicate values calculated only with coastal plain facies.

Tbins	P	NS	Occs	Tsp	Locs		Area		Rich		Ext		Ori		U	Chao
58 - 58.5	Pg	96	8752	0.5	17	(13)	79127	(79127)	158.11	(153.1)	0.077	(0.047)	0.103184	(0.114)	0.99	272.696
58.5 - 59	Pg	68	6012	0.5	22	(18)	90660	(90660)	133.75	(131.6)	0.01	(0)	0	(0)	0.99	177.087
59 - 59.5	Pg	59	4612	0.5	18	(17)	94315	(94315)	141.71	(138)	0.016	(0.051)	0.382992	(0.482)	0.99	212.333
59.5 - 60	Pg	39	3670	0.5	18	(14)	87848	(84713)	158.20	(136.3)	0.147	(0.134)	0.087011	(0.152)	0.98	234.364
60 - 61	Pg	24	2876	1	17	(9)	93430	(63238)	97.06	(76.6)	0.048	(0)	0.191891	(0.186)	0.98	185.028
61 - 62	Pg	18	1263	1	8	(5)	55583	(21666)	66.78	(42.3)	0.018	(-0.028)	0	(0)	0.98	83.25
62 - 63.5	Pg	29	1594	1.5	12	(8)	76278	(72835)	79.45	(53.8)	0.092	(0.098)	0.417735	(0.08)	0.98	121.118
63.5 - 65	Pg	15	1823	1.5	8	(7)	58245	(58245)	64.49	(57.9)	0	(0)	-0.04001	(0)	0.99	91.333
65 - 66	Pg	29	2828	1	8	(8)	62972	(62972)	112.93	(109.5)	0.173	(0.219)	0	(0)	0.98	186.065
66 - 66.5	M	51	3658	0.5	18	(17)	96601	(96601)	204.39	(206.9)	0.435	(0.472)	0.09685	(0.1)	0.97	434.613
66.5 - 67	M	24	2415	0.5	10	(10)	148684	(148684)	166.80	(167.8)	0	(0)	0.029559	(0.03)	0.97	300.111
67 - 67.5	M	38	3446	0.5	8	(7)	102272	(64259)	154.88	(153.1)	0	(0)	0	(0)	0.98	273.68
67.5 - 68	M	39	2824	0.5	11	(11)	139351	(139351)	207.62	(207.5)	0	(0.008)	-0.00939	(-0.029)	0.96	379.185
68 - 69	M	37	2523	1	11	(11)	43802	(43802)	214.13	(216)	0.137	(0.14)	0.200671	(0.213)	0.94	633.776
69 - 70	M	24	1322	1	8	(7)	42224	(19074)	158.80	(151.2)	-0.022	(-0.022)	0	(0)	0.94	378.375
70 - 71	M	22	1801	1	9	(9)	122534	(122534)	139.22	(138.2)	0	(0)	0.163325	(0.168)	0.96	244.48
71 - 72	M	25	1610	1	9	(8)	82285	(46267)	132.65	(124.5)	-0.05	(-0.067)	0.105361	(0.09)	0.96	315.036

Table S4
Effect of depositional environment on diversity indicators across the Maastrichtian–Paleocene interval, and correlations between diversity indicators, bin span and geographic area.

Comparison / test		TOTAL	Only coastal environment
Diversity	Mastrichtian (mean)	172.3	170.6
	Paleocene(mean)	84.1	68.0
	t.test (P-value)	**8.781e-05**	**0.0001089**
Diversity SQS 0.95	Mastrichtian (mean)	27.2	26.6
	Paleocene(mean)	12.7	10.8
	t.test (P-value)	**< 2.2e-16**	**< 2.2e-16**
Extinction rate	At 66 bin	0.44	0.47
	Mean other bins	0.04	0.04
Extinction SQS 0.95	At 66 bin	0.53	0.52
	Mean other bins	0.03	0.04
	t.test (P-value)	**< 2.2e-16**	**< 2.2e-16**
Origination rate	At 59 bin	0.38	0.48
	Mean other bins	0.09	0.08
Origination SQS 0.95	At 59 bin	0.28	0.32
	Mean other bins	0.08	0.08
	t.test (P-value)	**< 2.2e-16**	**< 2.2e-16**
Correlation between bin span and bin rates of origination	Spearman's rho	0.06	-0.02
	P-value	**0.813**	**0.945**
Correlation between bin span and bin rates of extinction	Spearman's rho	0.04	-0.14
	P-value	**0.890**	**0.600**
Correlation between geographic area and bin rates of origination	Spearman's rho	0.042	0.076
	P-value	**0.872**	**0.771**
Correlation between geographic area and bin rates of extinction	Spearman's rho	-0.179	0.044
	P-value	**0.493**	**0.867**

Table S5.
Location of leaf fossil sites of the Guaduas and Bogotá floras. Numbers in parenthesis indicate the number of quarries at each site. Data from the Cerrejón Fm. was taken from (*19*).

Formation	Site	Specimens	Coordinates	Location
Guaduas Fm.	Montecristo (7)	808 (census)	5.2357°N, 73.8042°W	Montecristo coalmine, Ubaté, Cundinamarca
Guaduas Fm.	Peñitas (2)	139	5.7428°N, 72.8551°W	Peñitas coalmine, Monguí, Boyacá
Guaduas Fm.	860017 (1)	165	5.558°N, 73.269°W	Chivatá, Boyacá
Guaduas Fm.	860017Ce	842 (census)	5.558°N, 73.269°W	Chivatá, Boyacá
Guaduas Fm.	860014 (1)	99	5.36°N, 73.634°W	Guachetá, Cundinamarca
Bogotá Fm.	Checua (14)	465	5.1375°N, 73.8467°W	Nemocón, Cundinamarca
Bogotá Fm.	Cogua (4)	581	5.0714°N, 73.9522°W	Cogua, Cundinamarca
Bogotá Fm.	0903Ce	1370 (census)	5.0767˚N, 73.9553°W	Cogua, Cundinamarca
Cerrejón Fm.	0315 – 0317 (2)	453	11.135° N, 72.570° W	Cerrejón coalmine, La Guajira
Cerrejón Fm.	0317Ce	423 (census)	11.135° N, 72.570° W	Cerrejón coalmine, La Guajira
Cerrejón Fm.	0318 – 0324 (5)	443	11.128° N, 72.555° W	Cerrejón coalmine, La Guajira
Cerrejón Fm.	0410 (1)	26	11.085° N, 72.688° W	Cerrejón coalmine, La Guajira
Cerrejón Fm.	0705 – 0712 (8)	370	11.130°N, 72.584°W	Cerrejón coalmine, La Guajira
Cerrejón Fm.	0705Ce	767 (census)	11.130°N, 72.584°W	Cerrejón coalmine, La Guajira

Table S6.
Familial affinities and size range of 45 leaf morphotypes of the Maastrichtian Guaduas leaf flora.

Morphotype	Size Range	Natural Affinities	Resemblance/Best Guess Family	Notes
GD1	Noto-Mesophyll	Rhamnaceae	Rhamnaceae	*Berhamniphyllum* sp.
GD2	Meso-Macrophyll			
GD3	Noto-Mesophyll		Dilleniaceae	
GD4	Meso-Macrophyll		Moraceae	
GD5	Mesophyll	Piperaceae	Piperaceae	*Piper margaritae* C.Martinez-Aguillon
GD6	Micro-Notophyll		Salicaceae	
GD7	Micro-Mesophyll	Lauraceae	Lauraceae	
GD8	Mesophyll		Cucurbitaceae	
GD9	Noto-Mesophyll		Malpighiaceae	
GD11	Mesophyll		Polygonaceae	
GD14	Mesophyll			
GD19	Mesophyll		Canellaceae	
GD20	Meso-Macrophyll			*"Ficus" andrewsii* Huert.
GD21	Noto-Mesophyll			
GD23	Noto-Mesophyll	Lauraceae	Lauraceae	
GD32	Noto-Mesophyll		Theaceae	
GD35	Noto-Mesophyll		Lauraceae	
GD50	Mesophyll			
GD52	Meso-Megaphyll		Urticaceae	*"Coussapoa" camargoi* Huert.
GD53	Micro-Notophyll			
GD54	Noto-Mesophyll			
GD55	Noto-Mesophyll			
GD56	Meso-Megaphyll		Hamamelidaceae	
GD58	Mesophyll			
GD59	Notophyll		Aristolochiaceae	
GD60	Macrophyll		Sapotaceae	
GD61	Macrophyll			
GD62	Macrophyll		Araceae	
GD63	Meso-Macrophyll			
GD64	Noto-Macrophyll		Aristolochiaceae	
GD65	Noto-Mesophyll		Monimiaceae	
GD66	Micro-Notophyll			
GD67	Mesophyll			
GD68	Micro-Mesophyll			
GD70	Micro-Mesophyll			
GD71	Micro-Mesophyll			
GD38			Cyclanthaceae	
GD40			Araceae	
GD41			Zingiberales	

GD46		Zingiberales	
GD47	Arecaceae		*Geonomites zipaquirensi*s Huert.
GD22	Polypodiaceae	Polypodiaceae	
GD33		Blechnaceae	
GD101	Polypodiaceae	Polypodiaceae	
GD103		Pteridaceae	

Table S7.
Familial affinities and size range of 48 leaf morphotypes of the Paleocene Bogotá leaf flora.

Morphotype	Size Range	Natural Affinities	Resemblance/Best Guess Family	Notes
BF4	Noto-Mesophyll	Malvaceae	Malvaceae	CJ26. *Malvaciphyllum* sp.
BF23	Micro-Mesophyll		Salicaceae	
BF33	Mesophyll	Euphorbiaceae	Euphorbiaceae	
BF34	Mesophyll			
BF36	Noto-Mesophyll		Ulmaceae	
BF37	Micro-Mesophyll		Euphorbiaceae	
BF2	Noto-Mesophyll		Salicaceae	
BF3	Mesophyll			
BF5	Micro-Mesophyll		Violaceae	
BF9	Mesophyll			
BF13	Noto-Macrophyll		Elaeocarpaceae	CJ43
BF31	Mesophyll			
BF35	Mesophyll	Theaceae	Theaceae	
BF50	Notophyll		Violaceae	CJ4
BF1	Mesophyll			
BF6	Mesophyll	Menispermaceae	Menispermaceae	CJ6
BF30	Notophyll			
BF32	Notophyll			
BF43	Micro-Mesophyll			
BF25	Nanophyll		Lauraceae	
BF7	Noto-Mesophyll	Lauraceae	Lauraceae	CJ22
BF8	Nanophyll			
BF10	Notophyll		Euphorbiaceae	CJ10
BF11	Notophyll			
BF12	Notophyll			CJ28
BF15	Notophyll			
BF16	Notophyll			
BF21	Lepto-Nanophyll	Fabaceae	Fabaceae	"Leaf Morphotype 2"
BF24	Notophyll			
BF26	Microphyll			
BF28	Mesophyll		Rhamnaceae	CJ21
BF29	Mesophyll			
BF38	Nano-Notophyll	Fabaceae	Fabaceae	"Leaf Morphotype 3"
BF39	Microphyll			
BF40	Notophyll	Canellaceae	Canellaceae/Winteraceae	
BF41	Mesophyll			
BF42	Micro-Notophyll			
BF44	Mesophyll	Lauraceae	Lauraceae	

BF51	Mesophyll			
BF52	Mesophyll			
BF27		Arecaceae	Arecaceae	CJ68
BF45		Zingiberales	Zingiberales	CJ49
BF46				
BF47				
BF48		Araceae	Araceae	CJ3. *Montrichardia aquatica*
BF49				
BF14				
BF22		Salviniaceae	Salviniaceae	*Salvinia bogotensis* A. Cuervo & N. Pérez

Table S8.
Precipitation estimates for the Guaduas, Bogotá, and Cerrejón floras based on leaf area analysis methods of Wilf et al. (*28*) and on the modern-day correlation of Peppe et al. (*29*).

	Wilf et al. (*28*)		**Peppe et al. (*29*)**	
	MAP (cm yr^{-1})	MAP ± standard error	MAP (cm yr^{-1})	MAP ± standard error
Guaduas	293	205 – 420	234	164 – 333
Bogotá	182	120 – 266	184	125 – 264
Cerrejón	308	213 – 441	240	167 – 343

Table S9.
Leaf mass per area (g m^{-2}) estimated for leaf morphotypes and sites. Data from Cerrejón flora was obtained from (*19*).

Site	Species	N	PW2A	LMA	Up	Low
Guaduas	GD6	13	0.0019	106.29	133.51	84.62
	GD53	11	0.0101	203.14	261.95	157.53
	GD32	10	0.0025	119.83	155.39	92.40
	GD21	10	0.0027	122.83	159.31	94.70
	GD52	9	0.0027	122.34	160.86	93.04
	GD23	6	0.0019	108.08	150.85	77.43
	GD22	6	0.0025	119.40	166.73	85.51
	GD7	5	0.0021	111.79	161.04	77.60
	GD9	4	0.0007	74.34	111.71	49.47
	GD35	4	0.0023	115.03	172.95	76.51
	GD70	4	0.0027	121.92	183.36	81.07
	GD3	4	0.0027	123.36	185.52	82.02
	GD54	3	0.0024	117.01	187.29	73.10
	GD71	3	0.0027	122.88	196.73	76.75
	GD14	2	0.0003	55.29	98.32	31.09
	GD19	2	0.0005	65.10	115.71	36.62
	GD11	2	0.0010	85.43	151.83	48.07
	GD59	2	0.0011	85.72	152.34	48.24
	GD68	2	0.0016	99.49	176.83	55.98
	GD4	2	0.0017	103.89	184.67	58.45
	GD2	1	0.0001	36.78	83.06	16.29
	GD40	1	0.0012	90.78	204.60	40.28
	GD1	1	0.0016	99.98	225.34	44.36
	GD33	1	0.0042	145.39	327.96	64.45
	Site Mean (N>1)	20	0.0022	121.08	134.29	109.17
Bogotá	BF37	16	0.0019	107.30	131.86	87.31
	BF13	12	0.0009	82.06	103.95	64.77
	BF21	8	0.0105	206.43	277.38	153.63
	BF7	4	0.0010	83.90	126.07	55.84
	BF36	4	0.0047	151.72	228.44	100.76
	BF15	3	0.0018	106.15	169.86	66.33
	BF23	3	0.0021	111.64	178.68	69.76
	BF11	3	0.0022	112.48	180.02	70.28
	BF26	2	0.0008	77.57	137.85	43.65
	BF39	2	0.0009	80.73	143.47	45.43
	BF5	2	0.0014	96.11	170.81	54.07
	BF38	2	0.0026	120.61	214.46	67.83
	BF10	2	0.0035	135.73	241.44	76.30
	BF1	1	0.0003	52.13	117.56	23.12
	BF44	1	0.0005	65.81	148.33	29.20

	BF3	1	0.0015	97.02	218.68	43.05
	BF42	1	0.0022	112.82	254.32	50.05
	BF25	1	0.0032	131.37	296.25	58.26
	Site Mean (N>1)	13	0.0023	128.39	144.66	113.95
Cerrejón	CJ01	9	0.0012	91.00	119.10	69.10
	CJ25	8	0.0011	87.00	115.60	64.90
	CJ22	5	0.0008	76.00	108.80	52.50
	CJ15	5	0.0011	86.00	124.50	60.10
	CJ08	4	0.0010	83.00	125.40	55.50
	CJ05	4	0.0015	98.00	148.00	65.50
	CJ02	3	0.0018	104.00	167.10	65.20
	CJ19	3	0.0020	108.00	173.60	67.80
	CJ06	2	0.0006	69.00	122.80	38.90
	CJ43	2	0.0006	70.00	124.40	39.40
	CJ13	2	0.0009	80.00	142.80	45.20
	CJ16	2	0.0010	83.00	146.90	46.50
	CJ04	2	0.0010	84.00	149.90	47.40
	CJ28	2	0.0011	88.00	156.50	49.50
	CJ38	2	0.0028	125.00	222.20	70.20
	CJ18	1	0.0002	44.00	99.20	19.50
	CJ17	1	0.0004	62.00	139.00	27.40
	CJ24	1	0.0006	70.00	158.80	31.30
	CJ50	1	0.0006	71.00	159.20	31.30
	CJ55	1	0.0007	74.00	166.80	32.80
	CJ10	1	0.0013	93.00	210.30	41.40
	CJ32	1	0.0014	95.00	213.20	42.00
	CJ21	1	0.0018	106.00	238.50	47.00
	CJ12	1	0.0029	126.00	283.80	55.80
	Site Mean (N>1)	15	0.0012	92.49	102.99	83.05

Table S10.
t-test difference of means for site-specific leaf mass per area at the Guaduas (Maastrichtian), Bogotá (Paleocene) and Cerrejón (Paleocene) floras.

	Difference of means	Std Error	t	d.f.	P
Guaduas – Bogotá	-7.31	5.10	-1.43	12	0.1772
Guaduas – Cerrejón	28.59	3.81	7.51	14	< 0.001
Bogotá – Cerrejón	35.06	4.98	7.22	12	< 0.001

Table S11.
Pairwise Wilcoxon test P-values comparing the fossil sites' dissimilarity indices with other. Fossil sites: Paleocene Pg1 = Cerrejón 0317Ce, Pg2 = Cerrejón 0705Ce, Pg3 = Bogotá 0903Ce; Maastrichtian: K1 = Guaduas Montecristo, K2 = Guaduas 860017Ce. Numbers in bold indicate Bonferroni-corrected *P* values, significant at $P<0.01$.

	BCI					**Amacayacu**			
	K1	K2	Pg1	Pg2		K1	K2	Pg1	Pg2
K2	0.033	-	-	-	K2	0.082	-	-	-
Pg1	**1.90e-09**	**2.00e-15**	-	-	Pg1	**< 2e-16**	**< 2e-16**	-	-
Pg2	**1.90e-10**	**4.00e-16**	1	-	Pg2	**< 2e-16**	**< 2e-16**	1	-
Pg3	**9.40e-06**	**9.30e-11**	1	0.236	Pg3	**8.60e-14**	**8.30e-11**	0.468	0.169

Data S1. (separate file)
Palynological counts.

Data S2. (separate file)
Leaf fossil collections from Guaduas and Bogotá Formations.

Data S3. (separate file)
Zircon- U/Pb isotopic data of sample D-928.

Data S4. (separate file)
Leaf morphotypes recovered from the Maastrichtian Guaduas flora.

Data S5. (separate file)
Leaf morphotypes recovered from the Paleocene Bogotá flora.

Data S6. (separate file)
Insect damage dataset.

Supplementary online files (Figshare digital repository, doi: 10.6084/m9.figshare.13611215)

File S1.
R code folder containing functions and scripts used in data analysis

File S2.
R file folder containing .csv and .txt data

File S3.
Folder containing python code for PyRate analysis

References and Notes

1. T. Westerhold, U. Röhl, T. Frederichs, C. Agnini, I. Raffi, J. C. Zachos, R. H. Wilkens, Astronomical calibration of the Ypresian timescale: Implications for seafloor spreading rates and the chaotic behavior of the solar system? *Clim. Past* **13**, 1129–1152 (2017). doi:10.5194/cp-13-1129-2017

2. V. Vajda, A. Bercovici, The global vegetation pattern across the Cretaceous – Paleogene mass extinction interval: A template for other extinction events. *Global Planet. Change* **122**, 29–49 (2014). doi:10.1016/j.gloplacha.2014.07.014

3. T. R. Lyson, I. M. Miller, A. D. Bercovici, K. Weissenburger, A. J. Fuentes, W. C. Clyde, J. W. Hagadorn, M. J. Butrim, K. R. Johnson, R. F. Fleming, R. S. Barclay, S. A. Maccracken, B. Lloyd, G. P. Wilson, D. W. Krause, S. G. B. Chester, Exceptional continental record of biotic recovery after the Cretaceous-Paleogene mass extinction. *Science* **366**, 977–983 (2019). doi:10.1126/science.aay2268 Medline

4. P. M. Hull, A. Bornemann, D. E. Penman, M. J. Henehan, R. D. Norris, P. A. Wilson, P. Blum, L. Alegret, S. J. Batenburg, P. R. Bown, T. J. Bralower, C. Cournede, A. Deutsch, B. Donner, O. Friedrich, S. Jehle, H. Kim, D. Kroon, P. C. Lippert, D. Loroch, I. Moebius, K. Moriya, D. J. Peppe, G. E. Ravizza, U. Röhl, J. D. Schueth, J. Sepúlveda, P. F. Sexton, E. C. Sibert, K. K. Śliwińska, R. E. Summons, E. Thomas, T. Westerhold, J. H. Whiteside, T. Yamaguchi, J. C. Zachos, On impact and volcanism across the Cretaceous-Paleogene boundary. *Science* **367**, 266–272 (2020). doi:10.1126/science.aay5055 Medline

5. K. R. Johnson, Extinctions at the antipodes. *Nature* **366**, 511–512 (1993). doi:10.1038/366511a0

6. V. D. Barreda, N. R. Cúneo, P. Wilf, E. D. Currano, R. A. Scasso, H. Brinkhuis, Cretaceous/Paleogene floral turnover in Patagonia: Drop in diversity, low extinction, and a *Classopollis* spike. *PLOS ONE* **7**, e52455 (2012). doi:10.1371/journal.pone.0052455 Medline

7. V. Vajda, J. I. Raine, Pollen and spores in marine Cretaceous/Tertiary boundary sediments at mid-Waipara River, North Canterbury, New Zealand. *N. Z. J. Geol. Geophys.* **46**, 255–273 (2003). doi:10.1080/00288306.2003.9515008

8. M. P. Donovan, A. Iglesias, P. Wilf, C. C. Labandeira, N. R. Cúneo, Rapid recovery of Patagonian plant-insect associations after the end-Cretaceous extinction. *Nat. Ecol. Evol.* **1**, 12 (2016). doi:10.1038/s41559-016-0012 Medline

9. A. Iglesias, P. Wilf, K. R. Johnson, A. B. Zamuner, N. R. Cúneo, S. D. Matheos, B. S. Singer, A Paleocene lowland macroflora from Patagonia reveals significantly greater richness than North American analogs. *Geology* **35**, 947–950 (2007). doi:10.1130/G23889A.1

10. D. J. Nichols, in *The Hell Creek Formation and the Cretaceous–Tertiary Boundary in the Northern Great Plains: An Integrated Continental Record of the End of the Cretaceous.* Geological Society of America Special Paper 361, J. H. Hartman, K. R. Johnson, D. J. Nichols, Eds. (2002), pp. 393–456.

11. D. J. Peppe, Megafloral change in the early and middle Paleocene in the Williston Basin, North Dakota, USA. *Palaeogeogr. Palaeoclimatol. Palaeoecol.* **298**, 224–234 (2010). doi:10.1016/j.palaeo.2010.09.027

12. S. L. Wing, J. Alroy, L. J. Hickey, Plant and mammal diversity in the Paleocene to Early Eocene of the Bighorn Basin. *Palaeogeogr. Palaeoclimatol. Palaeoecol.* **115**, 117–155 (1995). doi:10.1016/0031-0182(94)00109-L

13. E. J. M. Koenen, D. I. Ojeda, F. T. Bakker, J. J. Wieringa, C. Kidner, O. J. Hardy, R. T. Pennington, P. S. Herendeen, A. Bruneau, C. E. Hughes, The Origin of the Legumes is a Complex Paleopolyploid Phylogenomic Tangle closely associated with the Cretaceous-Paleogene (K-Pg) Mass Extinction Event. *Syst. Biol.* 10.1093/sysbio/syaa041 (2020). doi:10.1093/sysbio/syaa041 Medline

14. W. Wang, Rdel. C. Ortiz, F. M. B. Jacques, X.-G. Xiang, H.-L. Li, L. Lin, R.-Q. Li, Y. Liu, P. S. Soltis, D. E. Soltis, Z.-D. Chen, Menispermaceae and the diversification of tropical rainforests near the Cretaceous-Paleogene boundary. *New Phytol.* **195**, 470–478 (2012). doi:10.1111/j.1469-8137.2012.04158.x Medline

15. S. Ramírez-Barahona, H. Sauquet, S. Magallón, The delayed and geographically heterogeneous diversification of flowering plant families. *Nat. Ecol. Evol.* **4**, 1232–1238 (2020). doi:10.1038/s41559-020-1241-3 Medline

16. P. R. Renne, I. Arenillas, J. A. Arz, V. Vajda, V. Gilabert, H. D. Bermúdez, Multi-proxy record of the Chicxulub impact at the Cretaceous- Paleogene boundary from Gorgonilla Island, Colombia. *Geology* **46**, 547–550 (2018). doi:10.1130/G40224.1

17. V. Vajda-Santivanez, Miospores from upper Cretaceous-Paleocene strata in northwestern Bolivia. *Palynology* **23**, 181–196 (1999). doi:10.1080/01916122.1999.9989527

18. See the supplementary materials.

19. S. L. Wing, F. Herrera, C. A. Jaramillo, C. Gómez-Navarro, P. Wilf, C. C. Labandeira, Late Paleocene fossils from the Cerrejon Formation, Colombia, are the earliest record of Neotropical rainforest. *Proc. Natl. Acad. Sci. U.S.A.* **106**, 18627–18632 (2009). doi:10.1073/pnas.0905130106 Medline

20. J. Alroy, Colloquium paper: Dynamics of origination and extinction in the marine fossil record. *Proc. Natl. Acad. Sci. U.S.A.* **105** (suppl. 1), 11536–11542 (2008). doi:10.1073/pnas.0802597105 Medline

21. J. Alroy, The Shifting Balance of Diversity Aming Major Marine Animal Groups, The shifting balance of diversity among major marine animal groups. *Science* **329**, 1191–1194 (2010). doi:10.1126/science.1189910 Medline

22. J. Alroy, A more precise speciation and extinction rate estimator. *Paleobiology* **41**, 633–639 (2015). doi:10.1017/pab.2015.26

23. D. Silvestro, N. Salamin, A. Antonelli, X. Meyer, Improved estimation of macroevolutionary rates from fossil data using a Bayesian framework. *Paleobiology* **45**, 546–570 (2019). doi:10.1017/pab.2019.23

24. C. Jaramillo, M. J. Rueda, G. Mora, Cenozoic plant diversity in the neotropics. *Science* **311**, 1893–1896 (2006). doi:10.1126/science.1121380 Medline

25. C. Jaramillo, D. Ochoa, L. Contreras, M. Pagani, H. Carvajal-Ortiz, L. M. Pratt, S. Krishnan, A. Cardona, M. Romero, L. Quiroz, G. Rodriguez, M. J. Rueda, F. de la Parra, S. Morón, W. Green, G. Bayona, C. Montes, O. Quintero, R. Ramirez, G. Mora, S. Schouten, H. Bermudez, R. Navarrete, F. Parra, M. Alvarán, J. Osorno, J. L. Crowley, V. Valencia, J. Vervoort, Effects of rapid global warming at the Paleocene-Eocene boundary on neotropical vegetation. *Science* **330**, 957–961 (2010). doi:10.1126/science.1193833 Medline

26. A. Rangel, J. M. Moldowan, C. Niño, P. Parra, B. N. Giraldo, Umir Formation: Organic geochemical and stratigraphic assessment as cosource for Middle Magdalena basin oil, Colombia. *Am. Assoc. Pet. Geol. Bull.* **86**, 2069–2087 (2002).

27. M. A. Caccavari, Dispersión del polen en *Araucaria angustifolia* (Bert.) O. Kuntze. *Rev. Mus. Argent. Cienc. Nat.* **5**, 135–138 (2003). doi:10.22179/REVMACN.5.39

28. P. Wilf, S. L. Wing, D. R. Greenwood, C. L. Greenwood, Using fossil leaves as paleoprecipitation indicators: An Eocene example. *Geology* **26**, 203–206 (1998). doi:10.1130/0091-7613(1998)026<0203:UFLAPI>2.3.CO;2

29. D. J. Peppe, D. L. Royer, B. Cariglino, S. Y. Oliver, S. Newman, E. Leight, G. Enikolopov, M. Fernandez-Burgos, F. Herrera, J. M. Adams, E. Correa, E. D. Currano, J. M. Erickson, L. F. Hinojosa, J. W. Hoganson, A. Iglesias, C. A. Jaramillo, K. R. Johnson, G. J. Jordan, N. J. B. Kraft, E. C. Lovelock, C. H. Lusk, U. Niinemets, J. Peñuelas, G. Rapson, S. L. Wing, I. J. Wright, Sensitivity of leaf size and shape to climate: Global patterns and paleoclimatic applications. *New Phytol.* **190**, 724–739 (2011). doi:10.1111/j.1469-8137.2010.03615.x Medline

30. D. L. Royer, L. Sack, P. Wilf, C. H. Lusk, G. J. Jordan, Ü. Niinemets, I. J. Wright, M. Westoby, B. Cariglino, P. D. Coley, A. D. Cutter, K. R. Johnson, C. C. Labandeira, A. T. Moles, M. B. Palmer, F. Valladares, Fossil leaf economics quantified: Calibration, Eocene case study, and implications. *Paleobiology* **33**, 574–589 (2007). doi:10.1666/07001.1

31. I. J. Wright, P. B. Reich, J. H. C. Cornelissen, D. S. Falster, P. K. Groom, K. Hikosaka, W. Lee, C. H. Lusk, Ü. Niinemets, J. Oleksyn, N. Osada, H. Poorter, D. I. Warton, M. Westoby, Modulation of leaf economic traits and trait relationships by climate. *Glob. Ecol. Biogeogr.* **14**, 411–421 (2005). doi:10.1111/j.1466-822x.2005.00172.x

32. E. Correa, C. Jaramillo, S. Manchester, M. Gutierrez, A fruit and leaves of Rhamnaceous affinities from the late Cretaceous (Maastrichtian) of Colombia. *Am. J. Bot.* **97**, 71–79 (2010). doi:10.3732/ajb.0900093 Medline

33. C. Martínez, M. R. Carvalho, S. Madriñán, C. A. Jaramillo, A Late Cretaceous *Piper* (Piperaceae) from Colombia and diversification patterns for the genus. *Am. J. Bot.* **102**, 273–289 (2015). doi:10.3732/ajb.1400427 Medline

34. F. Herrera, M. R. Carvalho, S. L. Wing, C. Jaramillo, P. S. Herendeen, Middle to Late Paleocene Leguminosae fruits and leaves from Colombia. *Aust. Syst. Bot.* **32**, 385–408 (2019). doi:10.1071/SB19001

35. M. R. Carvalho, F. A. Herrera, S. Gómez, C. Martínez, C. Jaramillo, Eary records of Melastomataceae from the middle-late Paleocene rainforests of South America conflict with Laurasian origins. *Int. J. Plant Sci.* 10.1086/714053 (2021).

36. R. J. Burnham, Patterns in tropical leaf litter and implications for angiosperm paleobotany. *Rev. Palaeobot. Palynol.* **81**, 99–113 (1994). doi:10.1016/0034-6667(94)90129-5

37. R. Condit *et al.*, "Complete data from the Barro Colorado 50-ha plot: 423617 trees, 35 years, 2019 version." (2019); https://datadryad.org/stash/dataset/doi:10.15146/5xcp-0d46.

38. A. Duque, H. C. Muller-Landau, R. Valencia, D. Cardenas, S. Davies, A. de Oliveira, Á. J. Pérez, H. Romero-Saltos, A. Vicentini, Insights into regional patterns of Amazonian forest structure, diversity, and dominance from three large terra-firme forest dynamics plots. *Biodivers. Conserv.* **26**, 669–686 (2017). doi:10.1007/s10531-016-1265-9

39. C. Crifó, E. D. Currano, A. Baresch, C. Jaramillo, Variations in angiosperm leaf vein density have implications for interpreting life form in the fossil record. *Geology* **42**, 919–922 (2014). doi:10.1130/G35828.1

40. H. V. Graham, F. Herrera, C. Jaramillo, S. L. Wing, K. H. Freeman, Canopy structure in Late Cretaceous and Paleocene forests as reconstructed from carbon isotope analyses of fossil leaves. *Geology* **47**, 977–981 (2019). doi:10.1130/G46152.1

41. T. S. Feild, T. J. Brodribb, A. Iglesias, D. S. Chatelet, A. Baresch, G. R. Upchurch Jr., B. Gomez, B. A. R. Mohr, C. Coiffard, J. Kvacek, C. Jaramillo, Fossil evidence for Cretaceous escalation in angiosperm leaf vein evolution. *Proc. Natl. Acad. Sci. U.S.A.* **108**, 8363–8366 (2011). doi:10.1073/pnas.1014456108 Medline

42. C. K. Boyce, J.-E. Lee, T. S. Feild, T. J. Brodribb, M. Zwieniecki, Angiosperms Helped Put the Rain in the Rainforests: The Impact of Plant Physiological Evolution on Tropical Biodiversity. *Ann. Mo. Bot. Gard.* **97**, 527–540 (2010). doi:10.3417/2009143

43. M. R. Carvalho, P. Wilf, H. Barrios, D. M. Windsor, E. D. Currano, C. C. Labandeira, C. A. Jaramillo, Insect leaf-chewing damage tracks herbivore richness in modern and ancient forests. *PLOS ONE* **9**, e94950 (2014). doi:10.1371/journal.pone.0094950 Medline

44. K. J. Niklas, B. H. Tiffney, A. H. Knoll, in *Phanerozoic Diversity Patterns*, J. W. Valentine, Ed. (Princeton University Press, Princeton, NJ, 1985), pp. 97–128.

45. S. L. Wing, L. D. Boucher, Ecological Aspects of the Cretaceous Flowering Plant Radiation. *Annu. Rev. Earth Planet. Sci.* **26**, 379–421 (1998). doi:10.1146/annurev.earth.26.1.379

46. N. A. Jud, M. D. D'Emic, S. A. Williams, J. C. Mathews, K. M. Tremaine, J. Bhattacharya, A new fossil assemblage shows that large angiosperm trees grew in North America by the Turonian (Late Cretaceous). *Sci. Adv.* **4**, eaar8568 (2018). doi:10.1126/sciadv.aar8568 Medline

47. P. M. Barrett, Paleobiology of Herbivorous Dinosaurs. *Annu. Rev. Earth Planet. Sci.* **42**, 207–230 (2014). doi:10.1146/annurev-earth-042711-105515

48. S. L. Wing, in *Extinctions in the History of Life*, P. D. Taylor, Ed. (Cambridge Univ. Press, 2004), pp. 61–97.

49. M. Laurans, B. Hérault, G. Vieilledent, G. Vincent, Vertical stratification reduces competition for light in dense tropical forests. *For. Ecol. Manage.* **329**, 79–88 (2014). doi:10.1016/j.foreco.2014.05.059

50. L. F. Sarmiento-Rojas, in *Geology and Tectonics of Northwestern South America*, F. Cediel, P. Shaw, Eds. (Springer, 2019), pp. 673–747.

51. T. W. Walker, J. K. Syers, The fate of phosphorus during pedogenesis. *Geoderma* **15**, 1–19 (1976). doi:10.1016/0016-7061(76)90066-5

52. L. A. Cernusak, K. Winter, B. L. Turner, Transpiration modulates phosphorus acquisition in tropical tree seedlings. *Tree Physiol.* **31**, 878–885 (2011). doi:10.1093/treephys/tpr077 Medline

53. E. P. McDonald, J. E. Erickson, E. L. Kruger, Research note: Can decreased transpiration limit plant nitrogen acquisition in elevated CO2? *Funct. Plant Biol.* **29**, 1115–1120 (2002). doi:10.1071/FP02007 Medline

54. T. Jaffré, in *Conifers of the Southern Hemisphere*, N. J. Enright, R. S. Hill, Eds. (Melbourne Univ. Press, 1995), pp. 171–196.

55. D. A. Kring, D. D. Durda, Trajectories and distribution of material ejected from the Chicxulub impact crater: Implications for postimpact wildfires. *J. Geophys. Res. Planets* **107**, 5062 (2002). doi:10.1029/2001JE001532

56. D. Z. Epihov, S. A. Batterman, L. O. Hedin, J. R. Leake, L. M. Smith, D. J. Beerling, N_2-fixing tropical legume evolution: A contributor to enhanced weathering through the Cenozoic? *Proc. Biol. Sci.* **284**, 20170370 (2017). doi:10.1098/rspb.2017.0370 Medline

57. D. A. Coomes, R. B. Allen, W. A. Bentley, L. Burrows, C. D. Canham, L. Fagan, D. M. Forsyth, A. Gaxiola-Alcantar, R. L. Parfitt, W. A. Ruscoe, D. A. Wardle, D. J. Wilson, E. F. Wright, The hare, the tortoise and the crocodile: The ecology of angiosperm dominance, conifer persistence and fern filtering. *J. Ecol.* **93**, 918–935 (2005). doi:10.1111/j.1365-2745.2005.01012.x

58. W. J. Bond, The tortoise and the hare: Ecology of angiosperm dominance and gymnosperm persistence. *Biol. J. Linn. Soc. Lond.* **36**, 227–249 (1989). doi:10.1111/j.1095-8312.1989.tb00492.x

59. S. V. Wyse, Growth responses of five forest plant species to the soils formed beneath New Zealand kauri (*Agathis australis*). *N. Z. J. Bot.* **50**, 411–421 (2012). doi:10.1080/0028825X.2012.724428

60. W. A. Green, G. Hunt, S. L. Wing, W. A. DiMichele, Does extinction wield an axe or pruning shears? How interactions between phylogeny and ecology affect patterns of extinction. *Paleobiology* **37**, 72–91 (2011). doi:10.1666/09078.1

61. T. E. Wood, N. Takebayashi, M. S. Barker, I. Mayrose, P. B. Greenspoon, L. H. Rieseberg, The frequency of polyploid speciation in vascular plants. *Proc. Natl. Acad. Sci. U.S.A.* **106**, 13875–13879 (2009). doi:10.1073/pnas.0811575106 Medline

62. Z. Li, A. E. Baniaga, E. B. Sessa, M. Scascitelli, S. W. Graham, L. H. Rieseberg, M. S. Barker, Early genome duplications in conifers and other seed plants. *Sci. Adv.* **1**, e1501084 (2015). doi:10.1126/sciadv.1501084 Medline

63. J. D. Thompson, R. Lumaret, The evolutionary dynamics of polyploid plants: Origins, establishment and persistence. *Trends Ecol. Evol.* **7**, 302–307 (1992). doi:10.1016/0169-5347(92)90228-4 Medline

64. C. Montes, A. F. Rodriguez-Corcho, G. Bayona, N. Hoyos, S. Zapata, A. Cardona, Continental margin response to multiple arc-continent collisions: The northern Andes-Caribbean margin. *Earth Sci. Rev.* **198**, 102903 (2019). doi:10.1016/j.earscirev.2019.102903

65. C. Jaramillo, Dataset for "The end-Cretaceous and the origin of modern Neotropical rainforests data," figshare (2021); https://doi.org/10.6084/m9.figshare.13611215.v2.

66. A. Traverse, *Paleopalynology* (Publisher, ed. 2, 2007).

67. L. E. Edwards, Supplemented graphic correlation: A powerful tool for paleontologists and nonpaleontologists. *Palaios* **4**, 127–143 (1989). doi:10.2307/3514601

68. C. A. Jaramillo, M. Rueda, V. Torres, A palynological zonation for the Cenozoic of the Llanos and Llanos Foothills of Colombia. *Palynology* **35**, 46–84 (2011). doi:10.1080/01916122.2010.515069

69. L. E. Edwards, Insights on why graphic correlation (Shaw's method) works. *J. Geol.* **92**, 583–597 (1984). doi:10.1086/628893

70. A. B. Shaw, *Time in Stratigraphy* (McGraw-Hill, 1964).

71. K. O. Mann, H. R. Lane, in *Graphic Correlation, SEPM Special Publication*, K. O. Mann, H. R. Lane, Eds. (vol. 53., 1995), pp. 3–13.

72. J. L. Carney, R. W. Pierce, in *Graphic Correlation, SEPM Special Publication*, K. O. Mann, H. R. Lane, Eds. (1995), vol. 53, pp. 23–43.

73. R. A. Cooper *et al*., Quantitative biostratigraphy of the Taranaki Basin, New Zealand: A deterministic and probabilistic approach. *Am. Assoc. Pet. Geol. Bull.* **85**, 1469–1498 (2001).

74. C. Jaramillo, I. Romero, C. D'Apolito, G. Bayona, E. Duarte, S. Louwye, J. Escobar, J. Luque, J. D. Carrillo-Briceño, V. Zapata, A. Mora, S. Schouten, M. Zavada, G. Harrington, J. Ortiz, F. P. Wesselingh, Miocene flooding events of western Amazonia. *Sci. Adv.* **3**, e1601693 (2017). doi:10.1126/sciadv.1601693 Medline

75. K. C. Hood, GraphCor—Interactive Graphic Correlation Software (1998).

76. F. M. Gradstein, J. G. O. D. Schmitz, G. M. Ogg, Eds., *The Geologic Time Scale 2012* (Elsevier, 2012).

77. F. J. Hilgen *et al*., in *The Geologic Time Scale*, J. G. Gradstein, O. D. Schmitz, G. M. Ogg, Eds. (2012), pp. 923–978.

78. R Core Team, R: A language and environment for statistical computing (2018), (available at https://www.r-project.org/).

79. H.-G. Drost, Philentropy: Information Theory and Distance Quantification with R. *J. Open Source Softw.* **3**, 765 (2018). doi:10.21105/joss.00765

80. T. Galili, dendextend: An R package for visualizing, adjusting and comparing trees of hierarchical clustering. *Bioinformatics* **31**, 3718–3720 (2015). doi:10.1093/bioinformatics/btv428 Medline

81. M. Maechler, P. Rousseeuw, A. Struyf, M. Hubert, K. Hornik, cluster: Cluster Analysis Basics and Extensions (2019).

82. D. Boltovskoy, The range-through method and first-last appearance data in paleontological surveys. *J. Paleontol.* **62**, 157–159 (1988). doi:10.1017/S0022336000059060

83. O. Eilertsen, R. H. Okland, T. Okland, O. Pedersen, Data manipulation and gradient length estimation in DCA ordination. *J. Veg. Sci.* **1**, 261–270 (1990). doi:10.2307/3235663

84. J. Oksanen *et al*., Vegan: community ecology package. R package version 2.5-3. http://CRAN.R-project.org/package=vegan (2018).

85. A. T. Kocsis, C. J. Reddin, J. Alroy, W. Kiessling, The r package divDyn for quantifying diversity dynamics using fossil sampling data. *Methods Ecol. Evol.* **10**, 735–743 (2019). doi:10.1111/2041-210X.13161

86. J. Alroy, in *Quantitative Methods in Paleobiology*, J. Alroy, G. Hunt, Eds. (The Paleontological Society Papers, vol. 16, 2010), pp. 55–80.

87. M. Foote, Survivorship analysis of Cambrian and Ordovician trilobites. *Paleobiology* **14**, 258–271 (1988). doi:10.1017/S0094837300011994

88. R. J. Hijmans, geosphere: Spherical Trigonometry (2019); https://cran.r-project.org/package=geosphere.

89. G. Bayona, A. Cardona, C. Jaramillo, A. Mora, C. Montes, V. Valencia, C. Ayala, O. Montenegro, M. Ibañez-Mejia, Early Paleogene magmatism in the northern Andes: Insights on the effects of Oceanic Plateau-continent convergence. *Earth Planet. Sci. Lett.* **331–332**, 97–111 (2012). doi:10.1016/j.epsl.2012.03.015

90. B. Ellis *et al*., *Manual of Leaf Architecture* (Cornell Univ. Press, Ithaca, NY, 2009).

91. C. Raunkiaer, *The Life Forms of Plants and Statistical Plant Geography* (Clarendon, 1934).

92. L. J. Webb, A physiological classification of Australian rainforest. *J. Ecol.* **47**, 551–570 (1959). doi:10.2307/2257290

93. A. Das, A. Bucksch, C. A. Price, J. S. Weitz, ClearedLeavesDB: An online database of cleared plant leaf images. *Plant Methods* **10**, 8 (2014). doi:10.1186/1746-4811-10-8 Medline

94. G. G. Huertas, De la flora fosil de la Sabana. *Bol. Geol.* **5**, 53–57 (1960).

95. N. Pérez-Consuegra, A. Cuervo-Gómez, C. Martínez, C. Montes, F. Herrera, S. Madriñán, C. Jaramillo, Paleogene *Salvinia* (Salviniaceae) from Colombia and their paleobiogeographic implications. *Rev. Palaeobot. Palynol.* **246**, 85–108 (2017). doi:10.1016/j.revpalbo.2017.06.003

96. E. W. Berry, Tertiary fossil plants from Colombia, South America. *Proc. U. S. Natl. Mus.* **75**, 1–12 (1929). doi:10.5479/si.00963801.75-2795.1

97. R. Brown, Alterations in some fossil and living floras. *J. Wash. Acad. Sci.* **36**, 344–355 (1946).

98. O. Phillips, M. James, A. Gentry, *Global Patterns of Plant Diversity: Alwyn H. Gentry's Forest Transect Data Set* (Missouri Botanical Garden Press, St. Louis, 2002).

99. The Angiosperm Phylogeny Group *et al*., An update of the Angiosperm Phylogeny Group classification for the orders and families of flowering plants: APG IV. *Bot. J. Linn. Soc.* **181**, 1–20 (2016). doi:10.1111/boj.12385

100. A. Chao, R. L. Chazdon, R. K. Colwell, T. J. Shen, A new statistical approach for assessing similarity of species composition with incidence and abundance data. *Ecol. Lett.* **8**, 148–159 (2005). doi:10.1111/j.1461-0248.2004.00707.x

101. C. C. Labandeira, P. Wilf, K. R. Johnson, F. Marsh, *Guide to Insect (and Other) Damage Types on Compressed Plant Fossils. (Version 3.0—Spring 2007)* (Smithsonian Institution, Washington D.C., 2007).

102. A. Chao, R. L. Chazdon, R. K. Colwell, T. J. Shen, A new statistical approach for assessing similarity of species composition with incidence and abundance data. *Ecol. Lett.* **8**, 148–159 (2005). doi:10.1111/j.1461-0248.2004.00707.x

103. J. Sláma, J. Košler, D. J. Condon, J. L. Crowley, A. Gerdes, J. M. Hanchar, M. S. A. Horstwood, G. A. Morris, L. Nasdala, N. Norberg, U. Schaltegger, B. Schoene, M. N. Tubrett, M. J. Whitehouse, Plešovice zircon— A new natural reference material for U–Pb and Hf isotopic microanalysis. *Chem. Geol.* **249**, 1–35 (2008). doi:10.1016/j.chemgeo.2007.11.005

104. K. R. Ludwig, *User's Manual for Isoplot 3.00* (Berkeley Geochronology Center, Berkeley, CA, 2003).

105. J. M. Mattinson, Zircon U-Pb chemical abrasion ("CA-TIMS") method: Combined annealing and multi-step partial dissolution analysis for improved precision and accuracy of zircon ages. *Chem. Geol.* **220**, 47–66 (2005). doi:10.1016/j.chemgeo.2005.03.011

106. T. E. Krogh, A low contamination method for hydrothermal decomposition of zircon and extraction of U and Pb for isotopic age determination. *Geochim. Cosmochim. Acta* **37**, 485–494 (1973). doi:10.1016/0016-7037(73)90213-5

107. H. Gerstenberger, G. Haase, A highly effective emitter substance for mass spectrometric Pb isotope ratio determinations. *Chem. Geol.* **136**, 309–312 (1997). doi:10.1016/S0009-2541(96)00033-2

108. M. D. Schmitz, B. Schoene, Derivation of isotope ratios, errors and error correlations for U-Pb geochronology using 205Pb–235U–(233U)-spiked isotope dilution thermal ionization mass spectrometric data. *Geochem. Geophys. Geosyst.* **8**, Q08006 (2007). doi:10.1029/2006GC001492

109. D. J. Condon, R. B. Schoene, N. M. McLean, S. A. Bowring, R. Parrish, Metrology and traceability of U–Pb isotope dilution geochronology (EARTHTIME Tracer Calibration Part I). *Geochim. Cosmochim. Acta* **164**, 464–480 (2015). doi:10.1016/j.gca.2015.05.026

110. N. M. McLean, D. J. Condon, R. B. Schoene, S. A. Bowring, Evaluating uncertainties in the calibration of isotopic reference materials and multi-element isotopic tracers

(EARTHTIME Tracer Calibration Part II). *Geochim. Cosmochim. Acta* **164**, 481–501 (2015). doi:10.1016/j.gca.2015.02.040

111. A. H. Jaffey, K. F. Flynn, L. E. Glendenin, W. C. Bentley, A. Essling, Precision measurements of half-lives and specific activities of ^{235}U and ^{238}U. *Phys. Rev. C Nucl. Phys.* **4**, 1889–1906 (1971). doi:10.1103/PhysRevC.4.1889

112. J. L. Crowley, B. Schoene, S. A. Bowring, U-Pb dating of zircon in the Bishop Tuff at the millennial scale. *Geology* **35**, 1123–1126 (2007). doi:10.1130/G24017A.1

113. F. de la Parra, thesis, University of Florida (2009).

114. C. Jaramillo, O. Yepes-Amézquita, in *Estudios Geológicos del Valle Superior del Magdalena* (Universidad Nacional de Colombia, XVII., 1994), pp. 1–18.